Effect of Fibre Properties on the Structure, Strength, and Thermal Conductivity of Foam-Formed and Air-Laid Cellulosic Lightweight Fibrous Materials

Antti Koponen ,* Titta Kiiskinen , and Elina Pääkkönen

*Corresponding author: antti.koponen@vtt.fi

DOI: 10.15376/biores.20.4.10922-10958

GRAPHICAL ABSTRACT

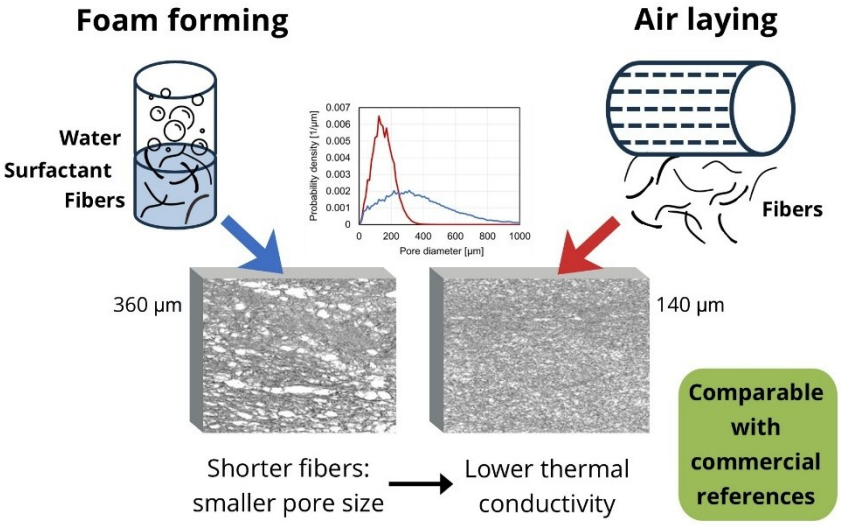

Effect of Fibre Properties on the Structure, Strength, and Thermal Conductivity of Foam-Formed and Air-Laid Cellulosic Lightweight Fibrous Materials

Antti Koponen ,* Titta Kiiskinen , and Elina Pääkkönen

The growing demand for sustainable materials is driving interest in cellulose fibres as eco-friendly alternatives to traditional insulation and cushioning materials, including expanded polystyrene (EPS), Extruded Polystyrene (XPS), and mineral wool, which pose environmental challenges. Foam forming has been extensively studied as a method for producing lightweight structures from cellulose fibres, but air-laying—a common nonwoven method—has been less explored. This study examines how wood fibre type and fibrillation level affect the structure, insulation, and strength of foam-formed and air-laid materials. A novel binding method is introduced for air-laying, involving post-laying water spraying to enhance bonding. Foam-formed materials had an average pore size of 300 to 600 µm with a wide distribution, including millimetre-scale pores; while air-laid materials had a smaller, more uniform pore size of 100 to 150 µm. Mechanical refining increased the pore size in foam-forming. Thermal conductivity decreased with decreasing fibre length, pore size, and increasing tortuosity of the fibre phase. The highest compression stress was achieved with refined chemi-thermomechanical pulp (CTMP), and the best recovery with unrefined bleached softwood kraft pulp (BSKP) and mixtures of acacia and BSKP. The findings suggest that mixing short hardwood fibres with longer softwood fibres in foam-forming could enhance performance in thermal insulation applications.

DOI: 10.15376/biores.20.4.10922-10958

Keywords: Cellulose fibres; Refining; Foam forming; Air-laying; X-ray microtomography; 3D structure; Pore size; Thermal conductivity; Strength properties

*Contact information: VTT Technical Research Centre of Finland Ltd, Koivurannantie 1, 40400 Jyväskylä, Finland; *Corresponding author: antti.koponen@vtt.fi*

INTRODUCTION

There is an increasing demand for sustainable alternatives to fossil-based materials across various applications and industries. In the construction industry, traditional insulation materials, such as expanded polystyrene (EPS), extruded polystyrene (XPS) and glass or mineral wool, are difficult to recycle and cause a significant environmental impact. The packaging industry is using increasingly cardboard-based solutions; however, cushioning is dominantly solved with various fossil-based materials, such as EPS, expanded polyethylene (EPE), and polyurethane. Replacing these materials with sustainable alternatives is challenging due to their excellent performance and properties: they are lightweight, durable, resistant to moisture and impact, and provide excellent thermal insulation.

Cellulose is an abundant, biodegradable, and renewable material, making it a natural candidate for sustainable insulation and cushioning materials (Hurtado *et al.* 2016; Fereira *et al.* 2021). While alternative sources for cellulose, such as agricultural side streams, exist and are intensively studied, wood fibres are still the most important source of cellulose for industrial applications. Wood fibres have well-established industrial processing methods and value chains. Depending on the application, chemical processing can produce relatively uniform, longer fibres, while mechanical processing results in shorter fibres with a broader length distribution. Additionally, refining can further modify fibre length and enhance fibrillation on fibre surfaces, influencing their bonding properties and overall performance.

One advantage of cellulose fibres is their ability to bond together by means of hydrogen bonds; no binders or glues are required to create strong and cohesive structures. This natural bonding ability enhances the sustainability of cellulose-based materials by eliminating the need for synthetic adhesives. This principle is widely utilised in the pulp and paper industry, where fibres are processed as an aqueous fibre suspension, and the fibres bond strongly during the drying phase. Dry fibres cannot create these bonds on their own, as hydrogen bonding relies on the presence of moisture.

For insulation and cushioning applications, lightweight, porous structures are required. In this case, wood fibres cannot be processed as aqueous suspensions, as the structures tend to collapse during dewatering and drying, even without a pressing phase (Zhu *et al.* 2022). More complex methods, such as freeze-drying (Ngyuen *et al.* 2014) or supercritical drying (Lopes *et al.* 2017), exist, but they are hardly practical for industrial-scale production.

Foam-forming (Hjelt *et al.* 2022; Nechita and Năstac 2022) is an alternative method for processing, *e.g.*, wood fibres. In the foam-forming process, fibres, water, and a foaming agent are mixed under high shear, creating fibre foam with an air content of approximately 60 to 70%. Once the fibre foam has been generated, it is placed onto a mesh screen, where part of the water drains away due to gravity, or by using a moderate vacuum, to prevent the collapse of the structure. Foam forming has some advantages over water forming: less water is needed during processing, bubbles prevent early fibre flocculation, which often leads to uniform structures, and it enables the use of materials that would otherwise settle in the water, forming non-uniform structures. Additionally, the bubbles support the fibre-foam structure during drying, resulting in the formation of lightweight fibrous materials with a density as low as 10 kg/m^3. This makes foam forming well-suited for making insulation (Pöhler 2017; Lecourt *et al.* 2018; Lohtander *et al.* 2022) and cushioning materials (Ottenhall *et al.* 2018; Pääkkönen *et. al* 2024). Other applications are also promising, such as sound insulation (Pöhler 2016; Nechita and Năstac 2018; Seciureanu *et al.* 2023), internal decoration (Härkäsalmi 2017; Siljander 2019) and filtration (Jahangiri *et al.* 2014).

In commercial cellulose fibre-based insulation products, the thermal conductivity typically ranges from 38 to 42 mW/m·K (Berge and Johansson 2012; Pöhler *et al.* 2017). For comparison, the thermal conductivity of air is 26 mW/m·K at 20 °C. In the review (Dominguez-Muñoz 2010), the thermal conductivity of insulation materials made of cellulosic fibres ranged between 35 and 45 mW/m·K in a set of 282 samples having a density between 17 and 115 kg/m^3. The best-performing cellulose fibre-based materials exhibit thermal conductivities comparable to those of glass wool, XPS, and EPS.

Several papers have reported thermal conductivities for lightweight foam-formed cellulosic fibre networks between 28 to 35 mW/m·K (Ngyen 2014; Seantier *et al.* 2016; Pöhler *et al.* 2017; Zhu *et al.* 2022; El Hajam *et al.* 2024; Hou *et al.* 2025). The lowest values have usually been achieved through the use of additives, such as microfibrillated cellulose or non-organic particles, and by more complex drying methods.

The mechanical properties of lightweight cellulose fibre materials are inferior compared to traditional polymer foams. Understanding the mechanical properties of foam-formed lightweight fibrous materials is thus important for their practical application (Alimadadi and Uesaka 2016; Ketoja *et al.* 2019; Burke *et al.* 2021; Wagner *et al.* 2025). To keep the materials biobased, reinforcement has been studied by adding fibrils, fines, cellulose micro/nanofibrils or biopolymers to the structure (Korehei *et al.* 2016; Li *et al.* 2016; Pöhler *et al.* 2020; Alonso *et al.* 2024).

An interesting research area is the 3D structure of the foam-formed fibrous materials (Al-Qararah *et al.* 2015; Burke *et al.* 2020; Pääkkönen *et al.* 2023). The ability to control the pore size distribution would enable fine-tuning the material properties according to the application. For example, a wide pore size distribution – particularly the presence of exceptionally large pores – can weaken the material's strength. Additionally, pore size distribution may affect the material's thermal insulation (Walle and Janssen 2019) and filtration properties (Chen *et al.* 2018). While many researchers have studied the 3D structures of their foam-formed materials, few authors have studied systematically its dependence on process parameters, fibre properties or additives.

Air-laying is a widely used process for creating nonwoven materials (Russel 2022; Paunonen *et al.* 2024). In this method, fibres are suspended in air and gradually collected onto a forming fabric. Because no water is involved, the drying phase is eliminated, resulting in significant energy savings. This makes air-laying an attractive option for processing wood fibres into lightweight, porous structures. However, the need for binders to hold the fibres together can limit its potential, as these binders may impact the material's recyclability and biodegradability.

In this study, the effect of wood fibre type and fibrillation level on the structure, thermal insulation properties, and strength properties of foam-formed and air-laid lightweight fibrous materials was examined. The dry air-laid fibre networks were bound by a novel procedure that involves spraying water into the dry structures after they have been air-laid.

EXPERIMENTAL

Furnishes

Table 1 presents the properties of furnishes and fibres used in this study. The Schopper Riegler (SR) degree was determined according to the EN ISO 5267-1 (2000) standard. The Canadian Standard Freeness (CSF) was measured according to the ISO 5267-2 (2001) standard. The conversions between the CSF and SR values were performed using the AFT freeness conversion chart (AFT 2018). The fibre length, fibre width, gravimetric coarseness, and the percentages of the A-type and B-type fines (flakes and fibrils type elements, See Appendix 1) were measured with the FS5 Fibre Image Analyzer (Valmet Automation, Kajaani, Finland).

Bleached softwood kraft pulp (BSKP) from Metsä Fibre (Äänekoski mill, Finland) was used at three SR levels. Here, traditional refining was performed at KCL (KCL Laboratory, Espoo, Finland). Bleached chemi-thermomechanical pulp (CTMP) from Metsä Fibre (Kaskinen mill, Finland) included 70 to 100% hardwood and 0 to 30% softwood and had the brightness (ISO 2470-1) of 82%, according to the manufacturer. Metsä Fibre CTMP was highly refined at VTT using a Masuko supermasscolloider (Masuko Sangyo Co., Ltd., Japan). Acacia furnish from April Asia was used both as such and as a 50% – 50% mixture (w/w) of acacia and unrefined BSKP. Refined CTMP was used both as is and in combination with a 4% (w/w) addition of TEMPO-oxidized cellulose nanofibrils (CNF), referred to subsequently as TEMPO. The TEMPO was obtained from Nippon Paper Industries Co. Ltd. as a 3% suspension. BSKP fluff pulp (BioBright untreated) from UPM Raumacell, obtained in a defibrated state, is primarily used for air-laid and hygiene products.

Microscopic images of the fibres are shown in Figs. 1 to 3. Note that the different fibre properties were not independent. The correlation between fibre length and fibre width was 0.40 (positive correlation), fibre width and coarseness 0.75 (positive correlation), and fibre length and coarseness 0.63 (positive correlation). This should be kept in mind when analysing the properties of the produced materials. In Table 1, the fibre properties were measured with the Valmet Fibre Image Analyzer (Valmet FS5). The values for the acacia-BSKP mixture were calculated with the formulae shown in Appendix 2. The SR values in parentheses were obtained from the AFT freeness conversion chart (AFT 2018).

Table 1. Used Furnishes, Freeness, Length Weighted Fibre Length, Fibre Width, Gravimetric Coarseness, and Fines A and B Percentages

Furnish	Freeness	Length (mm)	Width (µm)	Coarseness (mg/m)	Fines A (%)	Fines B (%)
BSKP	SR 16°	2.02	28	0.182	9.7	1.9
Refined BSKP	SR 23°	1.97	29	0.202	13.2	2.4
Highly refined BSKP	SR 89°	1.50	29	0.142	27.1	16.0
Acacia	SR 24°	0.80	14	0.065	16.7	2.6
Acacia 50%, BSKP 50%	-	1.12	18	0.096	13.2	2.3
CTMP	470 mL (SR 27°)	0.73	24	0.155	23.9	9.0
Refined CTMP	60 mL (SR 77°)	0.60	24	0.121	43.6	10.1
BSKP fluff	-	1.90	27	0.202	11.0	0.4

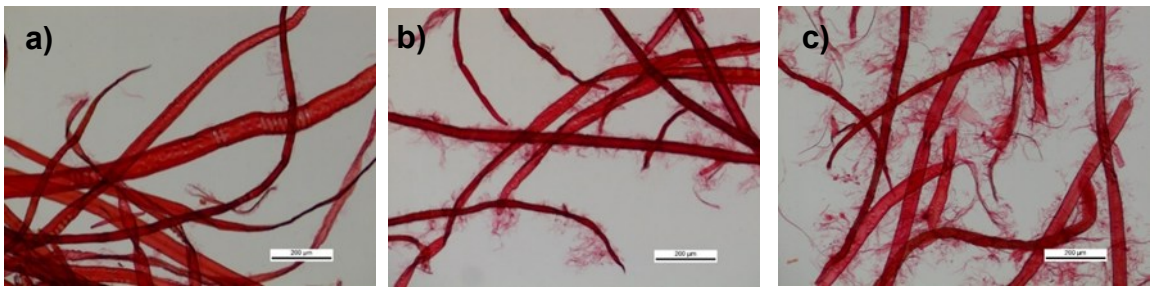

Fig. 1. Microscopic images of a) unrefined BSKP (SR16), b) refined BSKP (SR23), c) highly refined BSKP (SR89); The scale bar is 200 µm long.

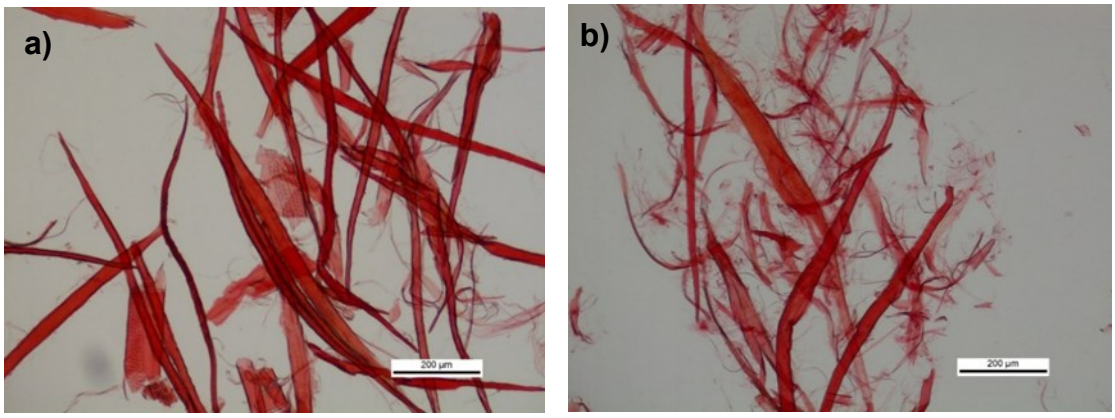

Fig. 2. Microscopic images of a) CTMP, b) highly refined CTMP; The scale bar is 200 µm long.

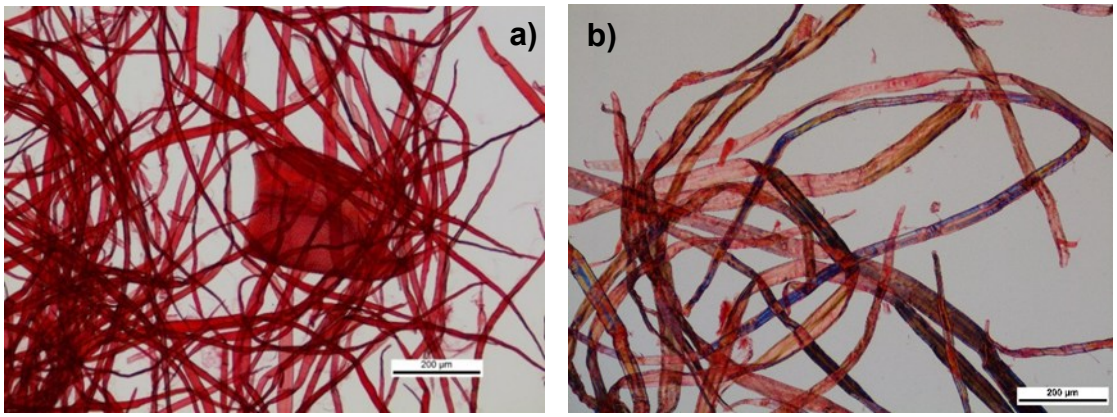

Fig. 3. Microscopic images of a) acacia b) BSKP fluff; The scale bar is 200 µm long

Foam Forming of Samples

The target sample density and thickness were 30 kg/m^3 and 30 mm, respectively, resulting in a target basis weight of 900 g/m^2. Three parallel samples were made for each trial point. The samples were made at room temperature (21 ºC).

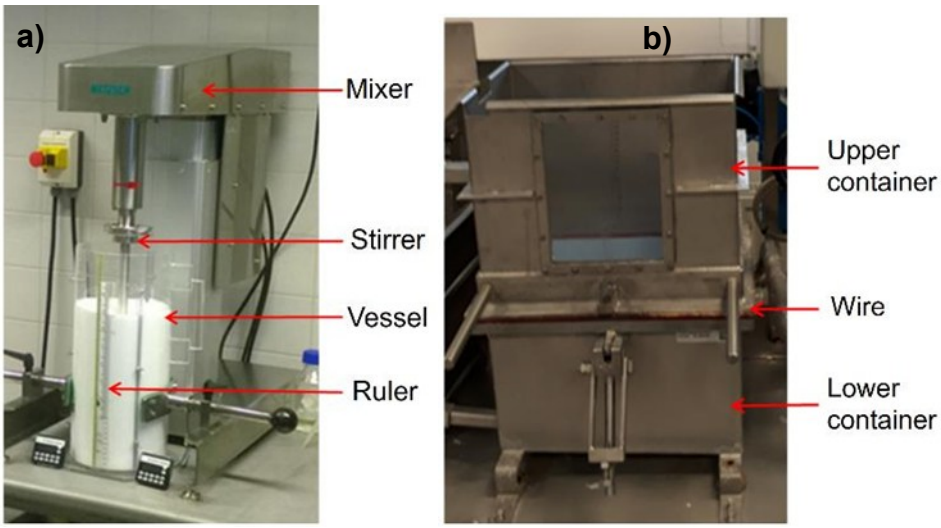

Fig. 4. a) Experimental set-up for the preparation of the fibre foams; b) Foam-forming sheet mould (Keränen *et al.* 2023)

The furnish was placed in a vessel with tap water and surfactants, and the fibre foam was generated using a laboratory mixer (Netzsch, Denmark, see Fig. 4a). The tap water at Jyväskylä, where the experiments were performed, is soft; salinity was 20 to 50 mg/L. As the surfactant, a mixture of sodium dodecyl sulphate (SDS) 0.6 g/L and polysorbate 20 (Tween 20) 0.6 g/L was used. Through using a co-surfactant with the SDS, the foaming agent residue in the foam-formed materials can be minimised (Viitala *et al.* 2020). The average foam bubble diameter was not measured but was likely of the order of 100 µm (Mira 2014; Koponen *et al.* 2020). Forming consistency was, in most cases, 3.5%. For acacia, the forming consistency was 4.4%, as retention was too low with 3.5% consistency (the basis weight of the final sample was only 80% of the target value). For refined CTMP, the forming consistency was 2.5% due to the high viscosity of the refined CTMP suspension. The water removal was also slow from the refined CTMP samples.

The target air content of the fibre-laden foam was 60%. In practice, the air content of wet foams varied between 57 to 67%. The foam generation time was kept constant at 8 min, with a rotational speed varying between 2000 to 4900 rpm, depending on the furnish type. The generated foam was poured along a tilted plane into a 33 cm × 24 cm handsheet mould (see Fig. 4b). The foam was left to drain in ambient conditions, while slightly pressing. The samples were dried overnight at 70 °C in an oven. The dried sheets were rewetted to reach a solid content of 50% by spraying water on the top and bottom surfaces of the sheet. The samples were placed in plastic bags, and the moisture content was allowed to balance for 4 h, turning the samples after 2 h. The samples were then compressed between metal plates to the target thickness and dried overnight at 70 °C in the oven. Before thermal conductivity measurements, the samples were cut to the size of 15 cm × 15 cm. Thermal conductivity was measured for two samples with densities that were closest to the target density and/or having the least variation in their thickness. For the compression stress measurement, five parallel samples were evaluated. The samples were cut from one sheet and had the size of 50 mm × 50 mm (25 cm^2) and the thickness of 27 to 30 mm.

Air Laying of Samples

The air-laid samples were prepared by using an air-laid laboratory drum former (Walkisoft, Anpap), as shown in Fig. 5. The relative humidity in the laboratory was 32 to 45% and the temperature was T=23 °C. Fluff fibres were pre-separated using a kitchen blender for 8 s. These fibres were then placed into a rotating cylindrical drum with rectangular gaps, which sieved the fibres onto a forming wire using airflow. A rotational speed of 60 rpm was used. The forming time was 5 min while changing the rotation direction three times, starting with a clockwise direction. The airflow speed through the device was controlled by a flow limiter valve, with setting values ranging from two to eight (lower values correspond to higher airflow). In this work, a setting of two was used. Towards the end of the forming time, the remaining fibres in the drum were forced through the rectangular gaps with compressed air while rotating to achieve the desired grammage of 450 g/m^2 for the sheets. The thickness of the obtained sheets was approximately 45 mm.

In contrast to foam forming, the final samples of air laying were obtained by overlapping two or three sheets and bonding them into a single sheet. The 30 kg/m^3 sample was composed of two sheets, combined to reach a total target basis weight of 900 g/m^2. The resulting sample was moistened to a 50% moisture content by spraying water on both sides. It was subsequently compressed to a thickness of 30 mm and dried overnight at 70 °C between forming mesh screens, plastic plates, and metal plates. The 45 kg/m^3 sample was composed of three sheets, resulting in a total target basis weight of 1350 g/m^2. After

combining and moistening the sample, it was sealed in a plastic bag for 4 h to allow the moisture to equilibrate. The sample was compressed and dried following the same procedure as the 30 kg/m³ sample.

Notice that instead of using water spray to moisten the airlaid sheets, fibres or airlaid sheets could potentially be moistened with gas or steam, as suggested in the patent (Kiiskinen *et al.* 2023).

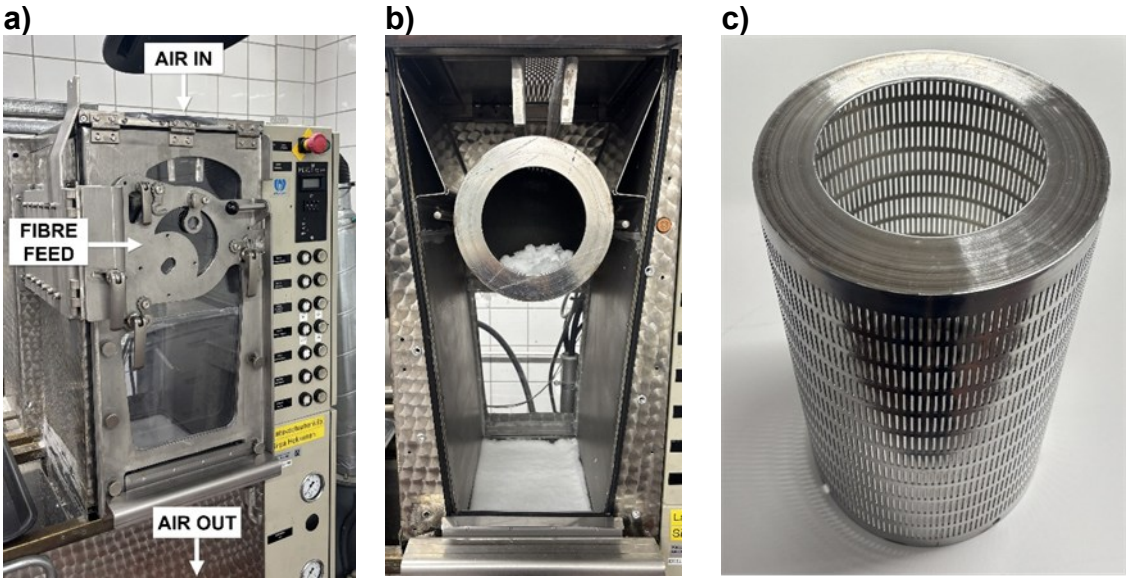

Fig. 5. a) The air-laying laboratory device; b) The chamber of the air-laying device with fibres in the drum and at the bottom a formed sheet on the wire; c) A close-up image of the rectangular gap drum into which the fibres were fed at the start of the operation.

X-ray Microtomography

Three-dimensional (3D) images of the fine-scale structure of the studied materials were obtained using X-ray tomography with an Rx Solutions Desktom 130 scanner (Chavanod, France). Samples of 2 × 2 × 3 cm^3 (these are x, y, and z-dimensions) were cut from regions with the most homogeneous structure. The imaging voxel size was 11.8 µm, but the images were scaled down to approximately 24 µm for the calculations due to the large file size of the volume data. From the 3D images, it was possible to calculate the fibre orientation distributions, porosity profiles, pore size distributions, and geometric tortuosities for the materials. Details of the X-ray tomographic measurements and analyses are provided in Appendix 3.

Thermal Conductivity Measurements

Conduction of heat in a certain direction, through a material due to temperature differences, is described by Fourier's law,

$$Q = -\lambda A \frac{\Delta T}{L} \quad (1)$$

where Q is heat flux (unit W), A is the area under inspection (m^2), L is the thickness of the sample (m), ΔT (K) is the temperature difference over the sample, and λ (W/m·K) is the thermal conductivity of the material.

The thermal conductivity of the studied materials was measured with the heat flow meter HFM Fox314, see Fig. 6a. In this device, the studied material is placed between a

hot and cold plate. The upper cold plate is moved downwards until the plate has good contact with the studied material. In the authors' measurements, the temperatures of the cold and hot plates were set to 10 °C and 30 °C, respectively. Appendix 3 includes a discussion of the accuracy of the HFM method and the reasons for preferring it over other existing measurement methods.

The chamber size of the HFM Fox314 device is 30 cm × 30 cm, but the actual measurement area is 10 cm × 10 cm, and one can measure thermal conductivity for rather small samples. In such measurements, the rest of the chamber is filled with insulation material (see Fig. 6b). Foam rubber was used for this purpose, with a measured thermal conductivity of 38.6 mW/m·K. Consequently, the thermal conductivities measured for the 15 cm × 15 cm samples in this study were likely somewhat higher than the true values (see Appendix 3).

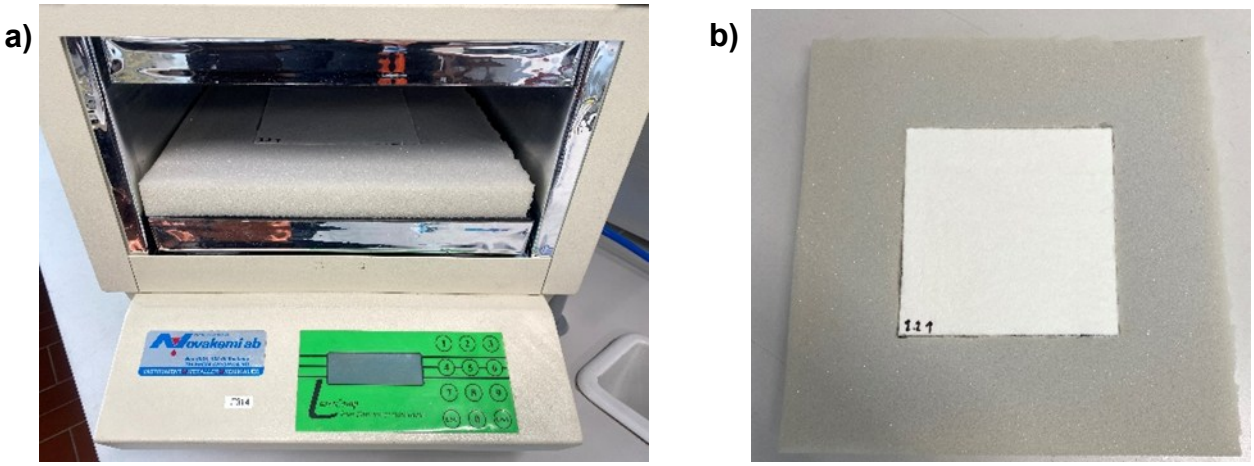

Fig. 6. a) Heat flow meter HFM Fox314; b) The chamber size of HFM Fox314 is 30 cm × 30 cm, but the actual measurement area is 10 cm × 10 cm. When measuring small samples (here 15 cm × 15 cm), the rest of the chamber was filled with foam rubber.

Measurement of Mechanical Properties

Compression stress was measured using a Lloyd R10K universal tester (Lloyd Instruments Ltd., Bognor Regis, West Sussex, UK). During the measurement, the sample was compressed to 50% of its initial thickness at a rate equal to its original thickness in mm per minute (speed mm/min). For the recovery measurement, the thickness of the sample was determined under a pressure of 250 Pa after it had recovered from compression for 1 min.

RESULTS AND DISCUSSION

Foam-Formed and Air-Laid Samples

Figure 7 shows cross-sections of various foam-formed and air-laid samples. Visual differences were observed in the uniformity and pore size of the samples, which varied depending on the furnishes used and/or the forming methods applied. Table 2 shows the density, pore size, and tortuosity in the solid phase, fibre orientation angle in the z-direction (vertical direction), and the thermal conductivity of the samples. The final densities were adjusted by rewetting and compressing the samples, but this was found challenging;

refining and the addition of TEMPO usually resulted in a higher final density during drying due to shrinking. Tortuosity in the void phase was less than 1.01 for all samples and is, therefore, not included in Table 2. In the following, tortuosity in the solid phase is referred to simply as 'tortuosity'.

Fig. 7. Cross-sections of various samples. Those containing BSKP fluff were prepared by air-laying, while all the others were foam-formed. There are five samples in each stack. The target shape of the samples was a rectangular prism.

Table 2. Density, Pore Size, and Tortuosity in the Solid Phase, Fibre Orientation Angle in the z-direction (Relative to the xy-plane), and Thermal Conductivity of the Samples

Sample	Density (kg/m^3)	Pore Size (μm)	Tortuosity in Solid	Fibre z-orientation (°)	Thermal Conductivity (mW/m·K)
BSKP	29.5	364	1.40	19.7	37.0
BSKP SR23	35.1	422	1.40	25.5	35.9
BSKP SR89	30.0	440	1.42	21.4	-
Acacia	29.4	325	1.40	16.3	34.2
Acacia + BSKP	32.0	346	1.31	24.5	35.9
CTMP	32.3	417	1.31	25.1	35.2
Refined CTMP	36.6	541	1.26	25.2	36.4
Refined CTMP + TEMPO	39.1	569	1.26	24.8	35.9
BSKP fluff-30 (air-laid)	28.7	142	1.47	28.0	35.1
BSKP fluff-40 (air-laid)	39.8	107	1.49	26.7	34.5

The density and thermal conductivity values were averaged over two samples. Notice that due to the sample unevenness, the BSKP SR89 sample was omitted from the thermal conductivity analysis.

Structural Analysis of Foam-Formed and Air-Laid Samples

Figures 8 to 10 show structural images in the mid-vertical plane for different furnishes (more structural images are presented in Appendix 4).

The average pore size, pore size inside the sample, and pore size at sample boundaries are shown in Fig. 11. Pore size inside the sample was calculated by excluding

the first 7 mm from both ends of the z-directional pore size profile (see the inset image in Fig. 11). Pore size at the sample boundaries was determined by averaging the z-directional porosity profile over the first and last 5 mm. Notice that the pore sizes of BSKP and CTMP were close to the values predicted by the formulae presented in Keränen *et al.* (2023), that give the average pore size as the function of density for lightweight foam-formed BSKP and CTMP materials.

It can be seen from Figs. 8 to 10 that the foam-formed structures were not homogeneous. There were many large voids, primarily caused by the merging of foam bubbles and fibres during forming and drying, as well as the non-optimal dispersion of the fibres. Moreover, both foam-formed and air-laid samples had a higher density (or lower porosity) on the upper and lower (wire side) boundaries. This can also be seen from the nominal porosity profiles shown in Fig. 12. Densification of the samples at their boundaries can occur both during forming (Lecourt *et al.* 2018; Burke *et al.* 2019; Keränen *et al.* 2023) and during compression after rewetting. The densification observed here was likely a combination of these two effects. Figure 13 shows z-directional pore size distributions for BSKP, CTMP, acacia, and BSKP fluff. It can be seen that, in all cases, pore size was smaller at the sample boundaries. Imaged samples were rather small when compared to the highest pore sizes, which explains the rather wide variation of the pore size in the distributions.

Figure 10c shows a structural image for the air-laid BSKP fluff-30 sample. The BSKP fluff-40 sample was similar (see Appendix 4). Compared to foam-formed samples, the structure of the air-laid samples was much more homogeneous, and the pore size was substantially smaller (see Fig. 11).

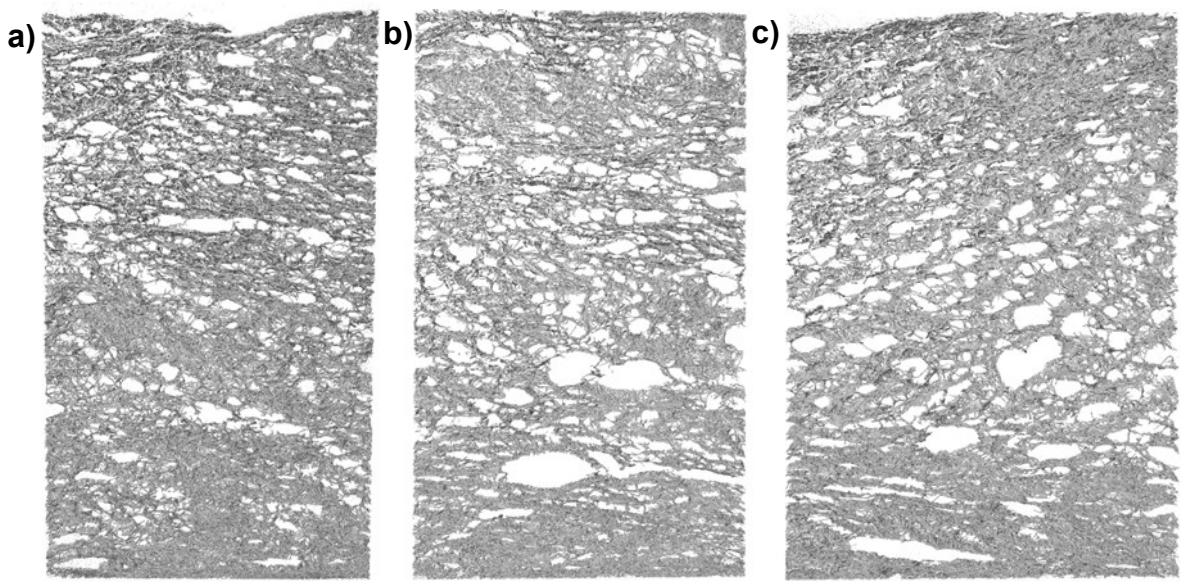

Fig. 8. Structural images for a) BSKP, b) BSKP SR23, and c) BSKP SR89; The image size is approximately 2 cm × 3 cm.

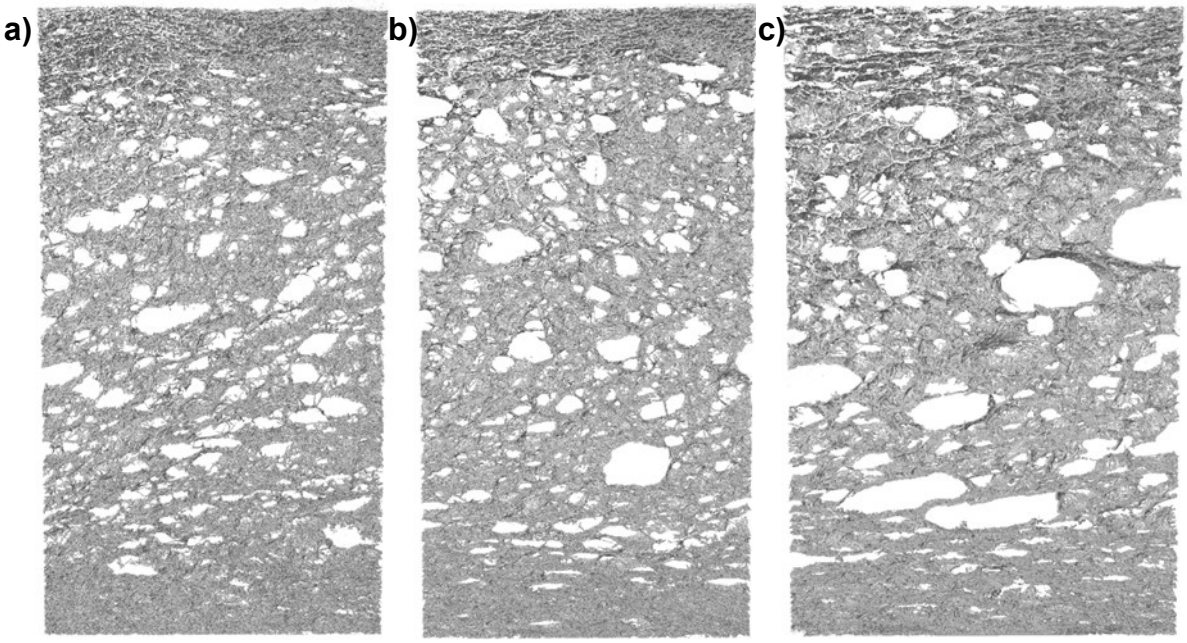

Fig. 9. Structural images for a) CTMP, b) refined CTMP, and c) refined CTMP + TEMPO samples; The image size is approximately 2 cm × 3 cm.

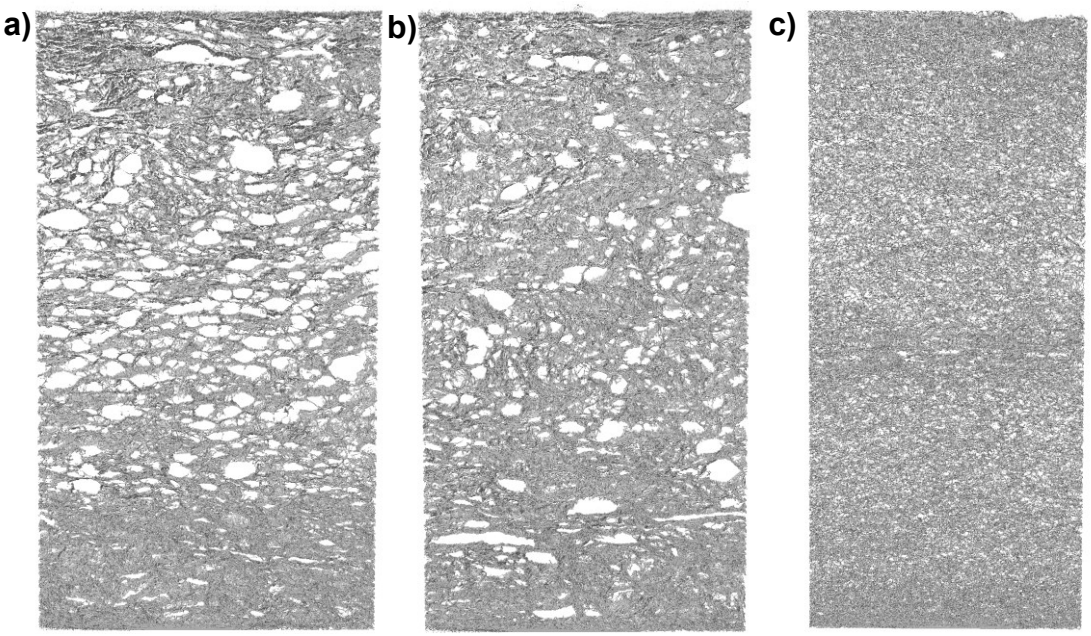

Fig. 10. Structural images for a) acacia and b) acacia-BSKP, c) air-laid BSKP fluff-30 sample. The structural image of BSKP fluff-40 sample was similar, but the pore size was even smaller (see Appendix 4). For a) and b), the image size is approximately 2 cm × 3 cm; for c) approximately 1.5 cm × 3 cm.

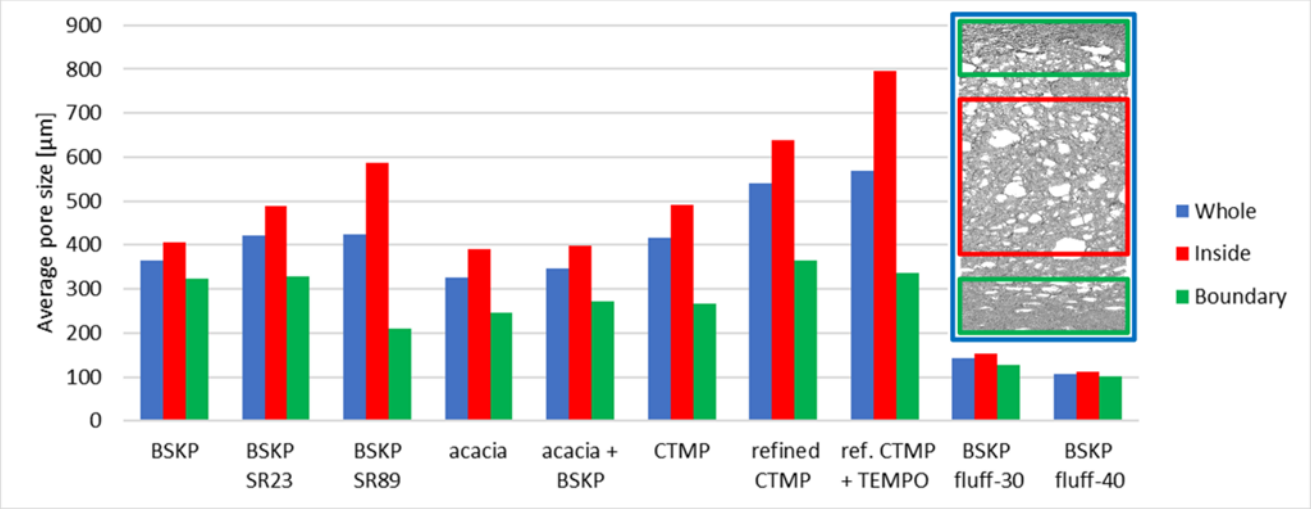

Fig. 11. The average pore size of the whole sample, inside the samples, and at the sample boundaries for the different furnishes. The inset image shows the regions where the average pore size in the whole sample (blue line), inside (red line), and at the boundaries (green line) has been calculated.

Figure 8 illustrates that the BSKP structures became more inhomogeneous with increased refining levels; simultaneously, the pore size also increased (see Fig. 11). The behaviour was rather similar for CTMP (see Fig. 9 and Fig. 11); the samples became more inhomogeneous, and the pore size increased with refining and when TEMPO nanocellulose was mixed into the furnish. This behaviour is somewhat surprising, as it is opposite to what is expected to happen during water forming, where refining tends to decrease the pore size of the dried samples (Goel *et al.* 2000; Helbrecht *et al.* 2023). Acacia had a slightly smaller pore size than BSKP, and combining acacia with BSKP resulted in only a marginally larger pore size than for pure acacia.

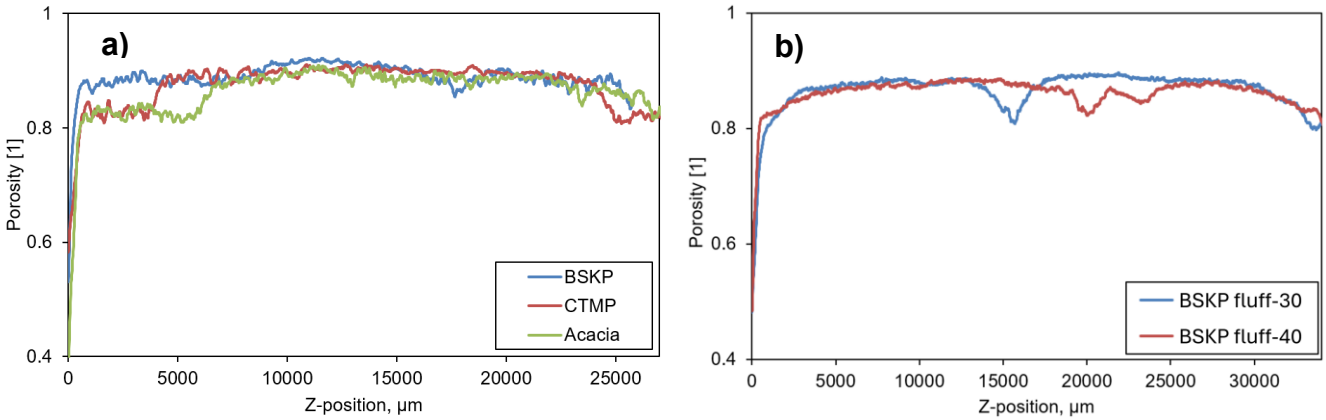

Fig. 12. Vertical (z-directional) nominal porosity profiles for a) BSKP, CTMP, and acacia, and b) air-laid BSKP fluff. The dips in porosity in the middle of the fluff samples are due to the samples being formed by joining separate pieces.

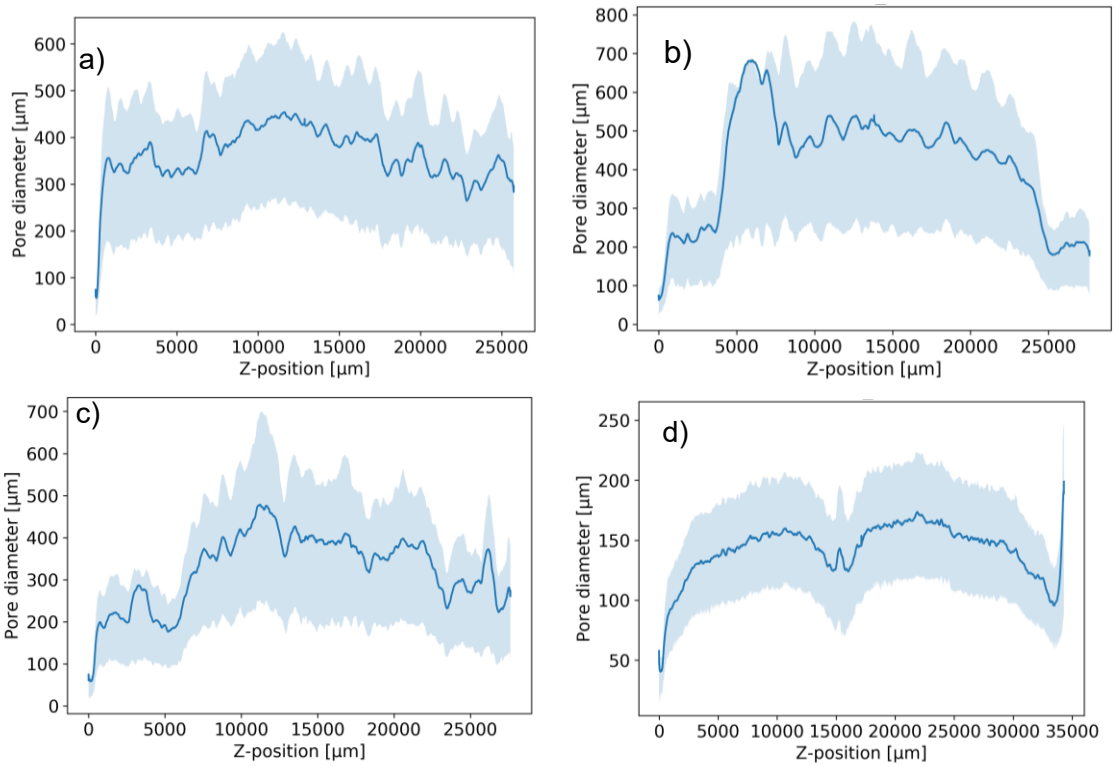

Fig. 13. Vertical (z-directional) pore size distributions for a) BSKP, b) CTMP, c) acacia, and d) air-laid BSKP fluff-30. The light blue colour shows the maximum and minimum of the pore size at each vertical position.

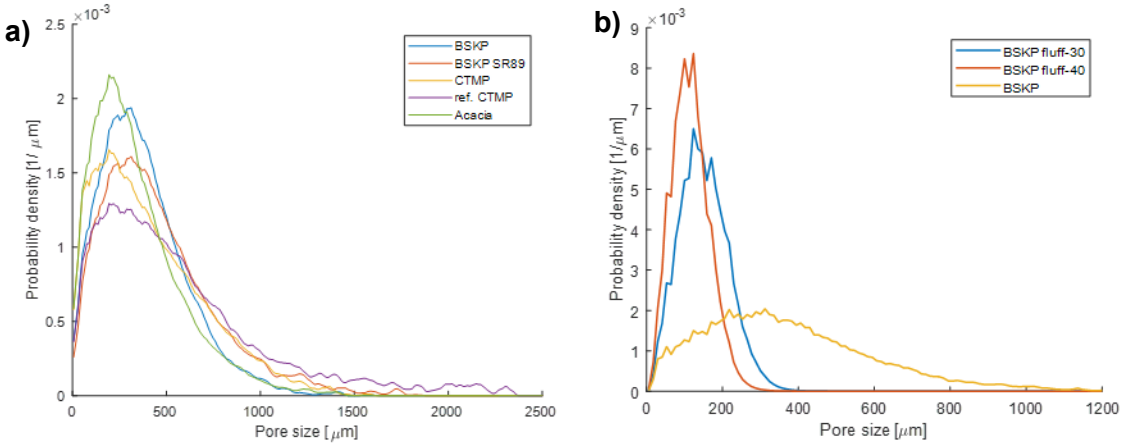

Fig. 14. a) Pore size distributions of various foam-formed samples. Some distributions were omitted, as they were similar to other distributions: acacia + BSKP (similar to acacia), BSKP SR23 (BSKP), and refined CTMP + TEMPO (refined CTMP). For clarity, the curves have been smoothed using a five-pixel moving average. b) Pore size distributions of air-laid BSKP fluff samples. For comparison, the pore size distribution of the foam-formed BSKP sample is also shown.

Figure 14a presents pore size distributions for different foam-formed samples (all pore size distributions are shown in Appendix 5). The distributions consist of two parts: a peak in the small pore region and a tail extending towards larger pore sizes, that can reach up to 2.5 mm. In the peak region, acacia exhibited the narrowest peak with the smallest

pore sizes. The maximum point for CTMP and refined CTMP occurred at the same location as with acacia, at 200 µm. For BSKP, and highly refined BSKP, the maximum was at 300 µm. Acacia and BSKP had similar tails, which were shorter than those of the other furnishes, with few pores larger than 1000 µm. Both CTMP and highly refined BSKP exhibited similar tails, with many pores in the 1000 to 1500 µm range. Refined CTMP had the longest tail, extending to nearly 2500 µm. Refining or addition of TEMPO CNF thus widened the pore size distribution and increased the number of large pores. The pore size distribution of air-laid samples is compared to that of foam-formed BSKP in Fig. 14b. The pore size distributions of air-laid samples were very narrow and, unlike those of foam-formed BSKP, did not have a long tail of large pores.

In fibre foams, the bubbles surround the fibres so that the fibres do not penetrate the bubble interiors, and the fibrils are located between the bubbles in the plateau borders and nodes (Hjelt *et al.* 2022). Initially, the bubbles inhibit the creation of fibre-fibre contacts, and the fibres are rather free to move during foam drainage, when the bubbles coarsen and coalesce. This enhances fibre packing, leading to localised fibre densification and the subsequent increase of pores. For this reason, the pore size distributions can be wide, and the samples can also include large pores. Fibrils generally strengthen fibre-fibre interactions, which may explain how refining or the addition of TEMPO CNF could enhance densification. It can be concluded that, in foam forming, increasing fibrillation or adding fibrils to the furnish does not necessarily reduce pore size without more advanced drying methods, such as freeze drying. However, this could depend on chemical factors, such as the surfactants used and the purity of the used water.

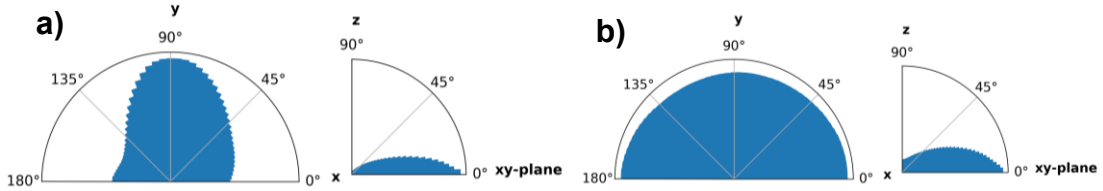

Fig. 15. Fibre orientation distributions on the xy-plane and to the z-direction for a) foam-formed BSKP, and b) air-laid BSKP fluff-30

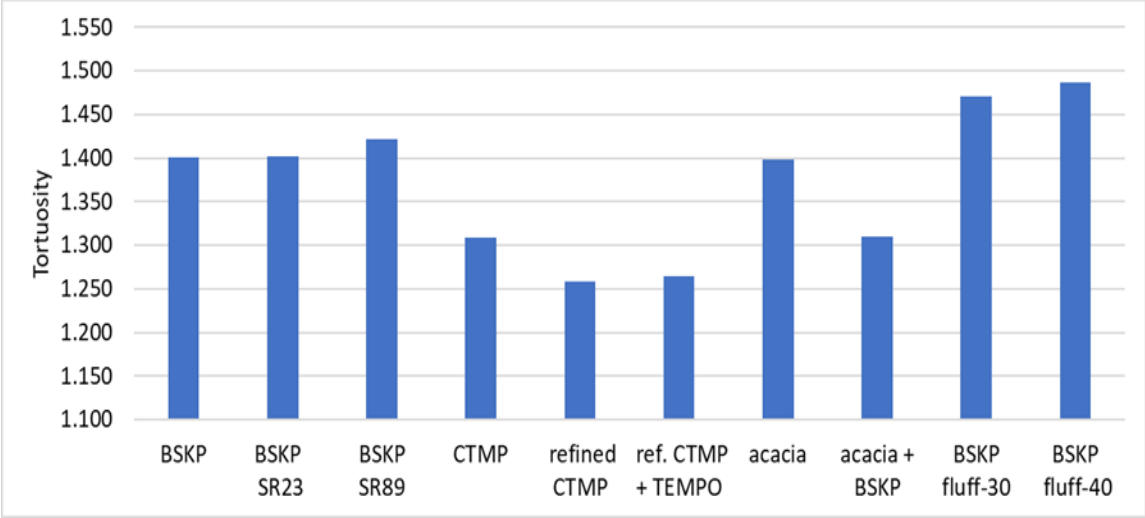

Fig. 16. The average tortuosity of samples made from different furnishes

Table 2 presents the average fibre orientation angle relative to the xy-plane (z-orientation) for all furnishes. There were no notable differences in z-orientation between the samples. In all cases, the fibres were predominantly oriented in the xy-plane for the foam-formed samples, aligning with the flow direction of the foam in the mould; whereas, air-laid fibres had no preferred direction on the xy-plane. Figure 15 shows, as an example, the fibre orientation distributions for foam-formed BSKP and air-laid BSKP fluff.

Tortuosity varied by 16% across the samples, as shown in Fig. 16 (see also Table 2). This variation is likely to impact the efficiency of thermal transport in the solid phase, as the effective thermal transport distance through the samples is proportional to their tortuosity.

Thermal Conductivity

Table 2 shows the thermal conductivity of samples made from different furnishes with foam forming or air laying. It can be seen that the difference between the lowest and highest thermal conductivity was 4.9 mW/m·K or 13% of their average. The differences were thus relatively small between the different furnishes.

Figure 17 shows the thermal conductivity as a function of density for different furnishes. The lowest thermal conductivity was obtained with foam-formed acacia and air-laid BSKP fluff. For comparison, the thermal conductivities of various commercial products are also shown. The best samples are seen to perform on par with them. The main reason for this is likely fibre orientation: there are fewer fibres in the z-direction, which slows down heat transfer through the solid phase in that direction (Uetani and Hatori 2017; see also Appendix 3). Mixing BSKP furnish with acacia increased the thermal conductivity, but it remained below that of pure BSKP. The effect of refining on thermal conductivity was not systematic; refining slightly decreased the thermal conductivity of BSKP samples but increased the thermal conductivity of CTMP samples.

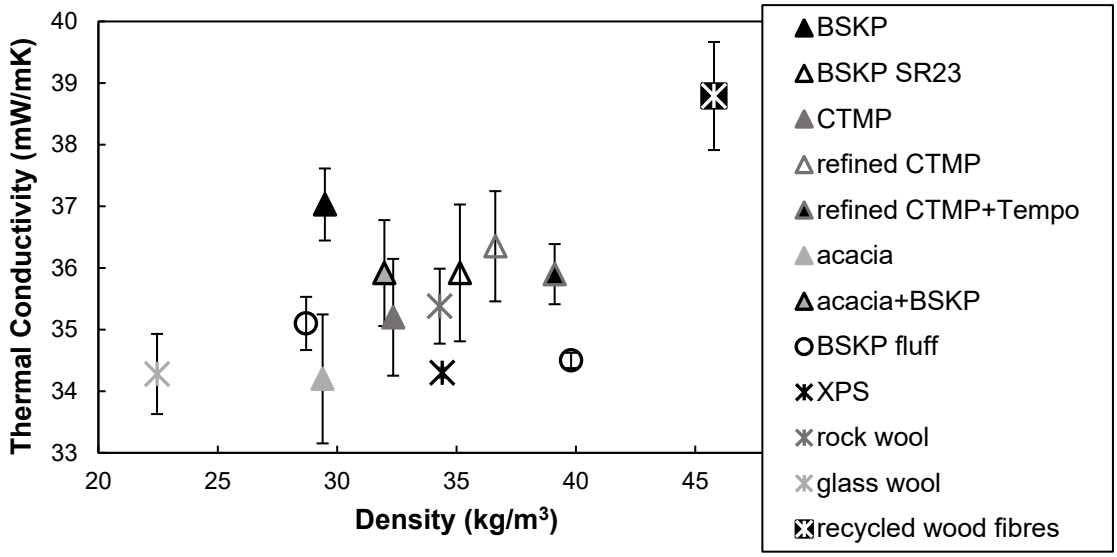

Fig. 17. Thermal conductivity as a function of density for different furnishes; Foam-formed samples are represented by triangles, air-laid samples by circles, and the commercial references for comparison by stars.

A linear regression analysis was performed with thermal conductivity (λ) as the dependent variable. As independent variables, two-variable combinations of fibre length, fibre width, coarseness, pore size, tortuosity, and z-orientation were tried. The strongest correlation was observed with fibre length (L) and tortuosity (T). This linear regression formula is described by Eq. 2,

$$\lambda = a + b \times L + c \times T \quad (2)$$

where a, b, and c are the regression coefficients. The obtained model parameters are presented in Table 3. The coefficient of determination was $R^2 = 0.87$. The p-value from the F-test for the overall model was 0.0025, indicating that the model was statistically significant.

Table 3. Regression Coefficients of Linear Regression Analysis for Thermal Conductivity, Eq. 2

Parameter	Value	p-value
a	56.9 ± 3.5	3.4×10^{-6}
b	2.01 ± 0.37	0.0016
c	-17.5 ± 2.8	0.00083

Many parameters showed significant correlations with one another: the correlation coefficient between tortuosity and pore size was -0.68 (negative correlation), tortuosity and fibre length 0.68 (positive correlation), and fibre length and pore size 0.40 (positive correlation); thus it is difficult to find the root mechanisms explaining the differences in the thermal conductivities of different samples. As an example, Fig. 18 shows that thermal conductivity generally increased with increasing pore size. Replacing tortuosity with pore size in Eq. 2 gave the coefficient of determination $R^2 = 0.68$, and the p-value from the F-test was 0.03.

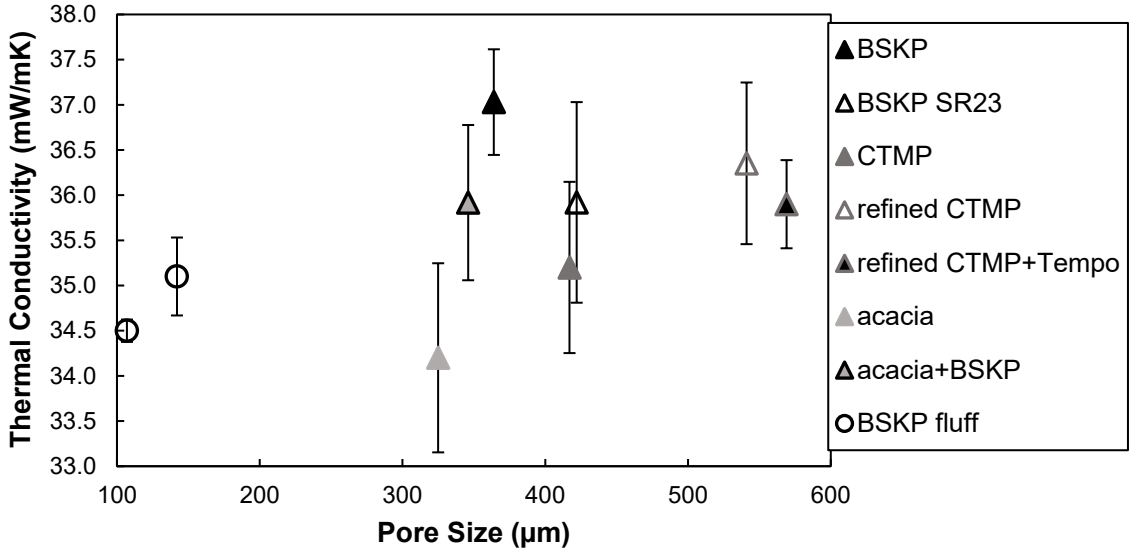

Fig. 18. Thermal conductivity for different furnishes as the function of average pore size; Foam-formed samples are represented by triangles and air-laid samples by circles.

Thermal conductivity is a combination of four components (Jelle 2011),

$$\lambda = \lambda_s + \lambda_g + \lambda_r + \lambda_{\text{conv}}, \quad (3)$$

where λ_s is due to thermal transport through the solid phase, λ_g is due to thermal transport through the pore space filled with air, and λ_r is due to thermal radiation through the pore space. Thermal transport due to convection, λ_{conv}, is usually omitted, as it becomes important for closed-cell and open-cell structures only when the pore size exceeds 4 mm and 2 mm, respectively (Alvarez-Lainez *et al.* 2008). Next, possible explanations for why thermal conductivity decreased with increasing tortuosity, decreasing fibre length, and decreasing pore size will be discussed (see Eq. 2).

Higher tortuosity reduces thermal transport efficiency in the solid phase, and shorter fibres shorten the mean free path of phonons (Feng *et al.* 2024). Both effects decrease λ_s. Here, pore size decreased both with decreasing fibre length and increasing tortuosity. Walle and Janssen (2019) studied numerically the effect of pore size on thermal radiation for porous materials. They found that the relative contribution of thermal radiation inside the pore space decreased significantly with decreasing pore size (the pore size varied between 1000 µm to 10 µm). Similarly, Lian *et al.* (2024) investigated the thermal conductivity of natural fibre-based porous materials using numerical simulations and found that the radiative thermal conductivity, λ_r, decreased monotonically as the pore size decreased from 400 µm to 1.0 µm, due to the shortening of the photon mean free path in the porous structures. They also found that λ_r decreased with decreasing fibre diameter, as a smaller diameter increases the number density of fibres per unit volume, providing more surface area to absorb thermal radiation (Scheiding 2000). Consequently, the observed decrease in thermal conductivity with decreasing fibre length can be attributed, at least in part, to the suppression of radiation. Fibre coarseness and fibre width are closely correlated with fibre length: lower coarseness and smaller fibre width both increase the total surface area of the fibre walls, enhancing the material's capacity to absorb thermal radiation.

In some high-end insulation materials, such as aerogels, low thermal conductivities are obtained by decreasing the pore size to utilise the Knudsen effect, which can significantly decrease λ_g. The Knudsen effect takes place when the pore size is below 10 µm, and between 10 µm and 1 µm pore sizes, the thermal conductivity decreases approximately 10% (Notario *et al.* 2015). A significant improvement in thermal insulation is only achieved with nanoscale pores. In the current case, the pore sizes were too large for the Knudsen effect to have much effect. Thermal transport through the air phase should be thus similar in all the samples, even more so as the tortuosity in the void phase was close to one for all samples.

Mechanical Properties

To evaluate the strength properties of foam-formed and air-laid sheets, the compression stress test was conducted. The maximum values for 50% compression and recovery after compression are presented in Table 4.

Figure 19 illustrates that the highest compression stress was achieved with highly refined CTMP hardwood fibre samples, while the addition of TEMPO CNF did not further improve results. The high compression results of those two CTMP samples may be explained by the increased fines content of refined CTMP. In a previous publication

(Pääkkönen *et al.* 2024), CTMP fines were seen to accumulate in inter-fibre joints and form film-like structures with a different CTMP grade. From the foam-formed samples, the sample made from acacia had the lowest compression stress, and it was marginally improved when the 50/50 mixture with BSKP was used. Refining of BSKP improved compression stress when compared to the structure made from unrefined BSKP. The air-laid samples exhibited the lowest compression stress values, but they were still higher when compared to commercial references. Upon the visual inspection and tactile assessment, it was determined that the fibre bonding of air-laid structures was insufficient, especially in the centre of the sample. Consequently, the lower compression stress values observed in air-laid samples, in comparison to foam-formed structures, may be attributed to the greater degree of collapse occurring from the centre rather than at the surfaces. This central collapse then predominantly influenced the overall stress response and recovery of the material.

The highest recovery (81.1%) was achieved with the unrefined BSKP sample and the sample made from a mixture of acacia and BSKP, and the poorest was with the samples having the highest strength, with the acacia sample and with the air-laid sample in the lower density level (Table 4).

Table 4. The Tested Trial Points, Densities, Compression Stress Maximum Values at 50% Compression, Density Normalised Compression Stress Results and the Recovery of the Compression

Trial Point	Density (kg/m^3)	Compression Stress max. (kPa)	st. dev.	Density Normalised Results* (kPa)	Thickness After Recovery (%)	st. dev.
BSKP	29.0	14.6	0.45	15.7	81.1	1.21
BSKP SR25	33.0	25.6	0.91	21.2	79.2	1.24
CTMP	32.2	21.5	0.87	18.7	77.7	2.11
Refined CTMP	28.4	52.2	2.73	58.1	76.8	1.17
Refined CTMP + TEMPO	28.6	53.1	3.99	58.4	78.3	2.21
Acacia	28.0	9.5	0.23	10.9	77.9	0.84
Acacia + BSKP	32.7	13.2	0.60	11.1	80.5	1.00
BSKP fluff-30 (air-aid)	26.2	5.4	0.51	7.1	75.6	0.98
BSKP fluff-40 (air-aid)	36.6	11.4	1.79	7.6	79.7	0.63
Rock wool	31.0	3.4	0.37	3.2	87.5	1.09
Recycled wood fibres	46.6	10.2	0.54	4.3	87.0	0.22

*Compression stress result normalised to the density level of 30 kg/m^3

Recovery after compression was 2.6 percentage points higher for the 50/50 acacia–BSKP mixture compared to pure acacia. Additionally, the difference in recovery between air-laid and foam-formed samples was surprisingly small. Similar to compression stress, the recovery also remained low for the lower-density air-laid sample, most likely because of the collapse of the poorly bonded inner structure. However, the recovery of the higher-density air-laid sample, with longer moistening time, was closer to the level of well-bonded foam-formed samples, which may indicate similar deformation mechanisms that reported for foam-formed samples (Ketoja *et al.* 2019; Pääkkönen *et al.* 2024). Compared to the studied materials, the reference materials exhibited higher recovery values (87 to 87.5%),

indicating potential areas for further improvements in foam- and airlaid materials. Further research on air-laid structures is required to enhance inter-fibre bonding, particularly in low-density materials.

Overall, these results, together with the thermal conductivity measurements and pore size analyses, suggest that, for foam-forming processes, combining short hardwood fibres with longer softwood fibres may provide the best overall performance in thermal insulation applications.

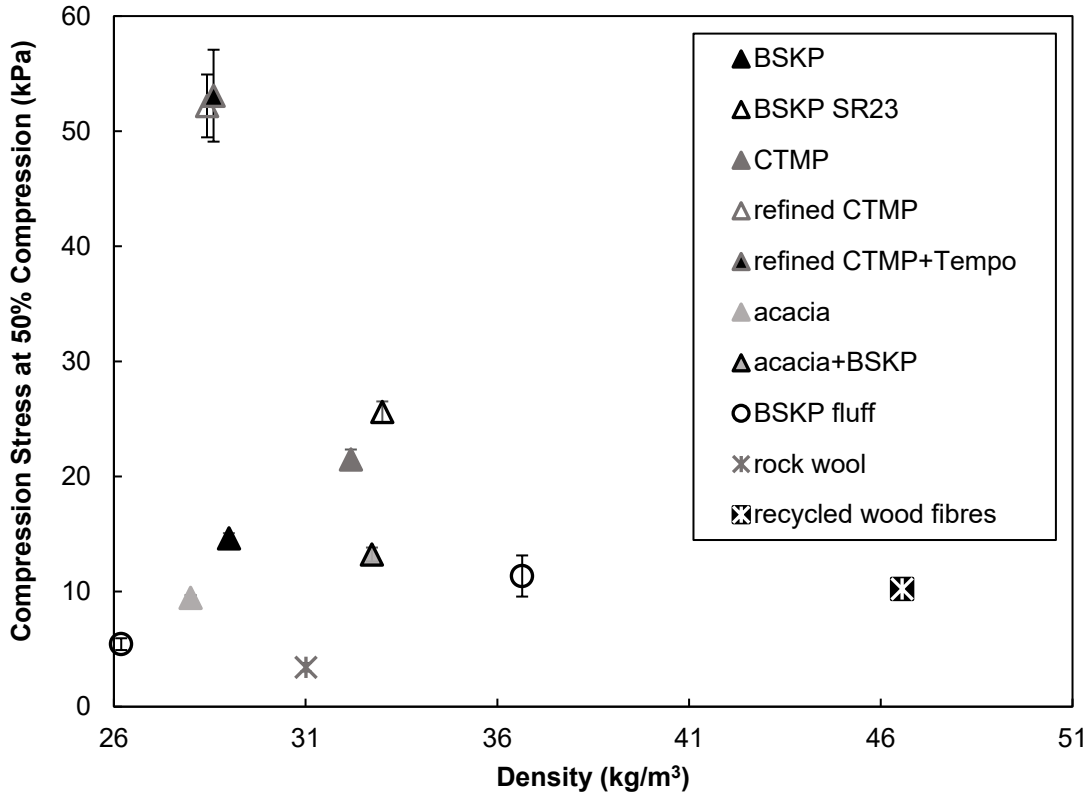

Fig. 19. The effect of different fibre types and forming methods on compression strength at -50% strain; Foam-formed samples are represented by triangles, air-laid samples by circles, and two commercial references for comparison by stars.

CONCLUSIONS

1. Mechanical refining increased the average pore size of foam-formed fibrous lightweight materials, primarily by introducing a long tail of large pores into the pore size distribution.
2. Air laying resulted in a narrower pore size distribution and a significantly smaller average pore size compared to foam forming.
3. Foam-formed and air-laid fibrous lightweight materials had excellent thermal insulation properties, with a relatively small difference in insulation performance across different furnishes.

4. The thermal conductivity of fibrous lightweight materials decreased with shorter fibre length, smaller pore size, and increased tortuosity.
5. The compression stress and recovery, along with thermal conductivity measurements and pore size analyses, indicate that combining short hardwood fibres with longer softwood fibres may result in optimal performance for thermal insulation applications made with the foam-forming process. Further research is required on air-laid structures to enhance inter-fibre bonding in low-density materials.

ACKNOWLEDGMENTS

This work was supported by the European Regional Development Fund under Grants A75938 and A80772 (Projects "Piloting Alternatives for Plastics" and "Energy First - Fibre Product Forming"). We would like to express our gratitude to Jukka Ketoja for his insightful suggestions and contributions to this text. We also thank Tuomas Turpeinen for his invaluable contribution to X-ray tomography and Juha Mannila for conducting the hot disk thermal conductivity measurements presented in Appendix 3.

USE OF AI-BASED LANGUAGE MODELS

AI-based language models ChatGPT (OpenAI, San Francisco, CA, USA), and Microsoft Copilot (Microsoft Corporation, Redmond, WA, USA) were used to improve readability and refine language in the manuscript. The AI was not used for data analysis, interpretation or scientific conclusions. The authors take full responsibility for the final content and any errors.

REFERENCES CITED

AFT (2018). "Pulp freeness conversion chart," AFT Global, (https://aft-global.com/en/resources/pulp-freeness-conversion-chart), Accessed 05 May 2025.

Alimadadi, M., and Uesaka, T. (2016). "3D-oriented fiber networks made by foam forming," *Cellulose* 23(1), 661-671. DOI: 10.1007/s10570-015-0811-z

Alonso, M., Hossain, R., El Hajam, M., and Tajvidi, M. (2024). "Enhancement of the physical and mechanical properties of cellulose nanofibril-reinforced lignocellulosic foams for packaging and building applications," *Nanomaterials* 14(22), article 1837. DOI: 10.3390/nano14221837

Al-Qararah, A., Ekman, A., Hjelt, T., Ketoja, J., Kiiskinen, H., Koponen, A., and Timonen, J. (2015). "A unique microstructure of the fiber networks deposited from foam-fiber suspensions," *Colloids and Surfaces A: Physicochemical and Engineering Aspects* 482, 544-553. DOI: 10.1016/j.colsurfa.2015.07.010

Alvarez-Lainez, M., Rodriguez-Perez, M., and de Saja, J. (2008). "Thermal conductivity of open-cell polyolefin foams," *Journal of Polymer Science Part B: Polymer Physics* 46(2), 212-221. DOI: 10.1002/polb.21358

Berge, A., and Johansson, P. (2012). *Literature Review of High Performance Thermal Insulation*," Department of Civil and Environmental Engineering," Division of

Building Technology, Building Physics, Chalmers University of Technology, Gothenburg, Sweden.

Burke, S., Möbius, M., Hjelt, T., Ketoja, J., and Hutzler, S. (2021). "Analysis of the foam-forming of non-woven lightweight fibrous materials using X-ray tomography," *SN Applied Sciences* 3, article 192. DOI: 10.1007/s42452-021-04172-9

Burke, S., Möbius, M., Hjelt, T., and Hutzler, S. (2019). "Properties of lightweight fibrous structures made by a novel foam forming technique," *Cellulose* 26, 2529-2539. DOI: 10.1007/s10570-018-2205-5

Chen, F., Ji, Z., and Qi, Q. (2018). "Effect of pore size and layers on filtration performance of coalescing filters with different wettabilities," *Separation and Purification Technology* 201, 71-78. DOI: 10.1016/j.seppur.2018.03.004

Domínguez-Muñoz, F., Anderson, B., Cejudo-López, J., and Carrillo-Andrés, A. (2010). "Uncertainty in the thermal conductivity of insulation materials," *Energy and Buildings* 42(11), 2159-2168. DOI: 10.1016/j.enbuild.2010.07.006

El Hajam, M., Sun, W., Hossain, R., Hafez, I., Howell, C., and Tajvidi M. (2024). "Surfactant-assisted foam-forming of high performance ultra-low density structures made from lignocellulosic materials and cellulose nanofibrils (CNFs)," *Industrial Crops and Products* 221, article 119357. DOI: 10.1016/j.indcrop.2024.119357

Feng, Y., Eun, J., Kim, S., and Kim, Y. (2024). "Evaluation of equivalent thermal conductivity for carbon fiber-reinforced bentonite through experimental and numerical analysis," *Computers and Geotechnics* 165, article ID 105880. DOI: 10.1016/j.compgeo.2023.105880

Fereira, E., Rezende, C., and Cranston, E. (2021). "Fundamentals of cellulose lightweight materials: Bio-based assemblies with tailored properties," *Green Chemistry* 23, 3542-3568. DOI: 10.1039/D1GC00326G

Goel, A., Tzanakakis, M., Huang, S., Ramaswamy, S., Choi, D., and Ramarao, B. (2000). "Characterization of the three-dimensional structure of paper using X-ray microtomography," *TAPPI Journal* 84(5), 407-411.

Härkäsalmi, T., Lehmonen, J., Itälä, J., Peralta, C., Siljander, S., and Ketoja, J. (2017). "Design-driven integrated development of technical and perceptual qualities in foam-formed cellulose fibre materials," *Cellulose* 24(11), 5053-5068. DOI: 10.1007/s10570-017-1484-6

Helbrecht, C., Langhans, M., Meckel, T., Biesalski, M., and Schabel, S. (2023). "Analyses of the effects of fibre diameter, fibre fibrillation, and fines content on the pore structure and capillary flow using laboratory sheets of regenerated fibres," *Nordic Pulp & Paper Research Journal* 38(3), 425-440. DOI: 10.1515/npprj-2022-0077

Hjelt, T., Ketoja, J., Kiiskinen, H., Koponen, A., and Pääkkönen, E. (2022). "Foam forming of fibre products: A review," *Journal of Dispersion Science and Technology* 43(10), 1462-1497. DOI: 10.1080/01932691.2020.1869035

Hou, F., Huang, M., Liu, M., Zhan, Y., Sun, Y., Xia, L., and Zhang, C. (2025). "Effect and action mechanism of inorganic particles on the properties of foam, foam-formed paper, and fiber reinforced silica aerogel composites," *Ceramics International*. DOI: 10.1016/j.ceramint.2025.03.112

Hurtado, P., Rouilly, A., Vandenbossche, V., and Raynaud, C. (2016). "A review on the properties of cellulose fibre insulation," *Building and Environment* 96, 170-177. DOI: 10.1016/j.buildenv.2015.09.031

Jahangiri, P., Korehei, R., Zeinoddini, S., Madani, A., Sharma, Y., Phillion, A., Martinez, M., and Olson, J. (2014). "On filtration and heat insulation properties of foam formed cellulose based materials," *Nordic Pulp & Paper Research Journal* 29(4), 584-591. DOI: 10.3183/npprj-2014-29-04-p584-591

Jelle, B. (2011). "Traditional, state-of-the-art and future thermal building insulation materials and solutions – Properties, requirements and possibilities," *Energy and Buildings* 43(10), 2549-2563. DOI: 10.1016/j.enbuild.2011.05.015

Keränen, J., Jetsu, P., Turpeinen, T., and Koponen, A. (2023). "Dewatering and structural analysis of foam formed lightweight fibrous materials," *BioResources* 18(1), 531-549. DOI: 10.15376/biores.18.1.531-549

Ketoja, J., Paunonen, S., Jetsu, P., and Pääkkönen, E. (2019). "Compression strength mechanisms of low-density fibrous materials," *Materials* 12(3), article 384. DOI: 10.3390/ma12030384

Kiiskinen, H., Pääkkönen, E., Paunonen, S., and Kiiskinen, T. (2023). "A process for dry-forming a fibrous raw material," FI20235613A1. (https://patents.google.com/patent/FI20235613A1)

Koponen, A., Timofeev, O., Jäsberg, A., and Kiiskinen, H. (2020). "Drainage of high-consistency fibre-laden foams," *Cellulose* 27(15), 9637-9652. DOI: 10.1007/s10570-020-03416-y

Korehei, R., Jahangiri, P., Nikbakht, A., Martinez, M., and Olson, J. (2016). "Effects of drying strategies and microfibrillated cellulose fiber content on the properties of foam-formed paper," *Journal of Wood Chemistry and Technology* 36(4), 235-249. DOI: 10.1080/02773813.2015.1116012

Lecourt, M., Pöhler, T., Hornatowska, J., Salmén, L., and Jetsu, P. (2018). "Density profiles of novel kraft pulp and TMP based foam formed thermal insulation materials observed by X-ray tomography and densitometry," *Holzforschung* 72(5), 397-403. DOI: 10.1515/hf-2017-0116

Li, S., Xiang, W., Järvinen, M., Lappalainen, T., Salminen, K., and Rojas, O. J. (2016). "Interfacial stabilization of fiber-laden foams with carboxymethylated lignin toward strong nonwoven networks," *ACS Applied Materials & Interfaces* 8(30), 19827-19835. DOI: 10.1021/acsami.6b06418

Lian, X., Tian, L., Li, Z., and Zhao, X. (2024), "Thermal conductivity analysis of natural fiber-derived porous thermal insulation materials," *International Journal of Heat and Mass Transfer* 220, article 124941. DOI: 10.1016/j.ijheatmasstransfer.2023.124941

Lohtander, T., Herrala, R., Laaksonen, P., Franssila S., and Österberg, M. (2022). "Lightweight lignocellulosic foams for thermal insulation," *Cellulose* 29, 185-187. DOI: 10.1007/s10570-021-04385-6

Lopes, J., Mustapa, A., Pantić, M., Bermejo, M., Martín, Á., Novak, Z., Knez, Ž., and Cocero, M. (2017). "Preparation of cellulose aerogels from ionic liquid solutions for supercritical impregnation of phytol," *The Journal of Supercritical Fluids* 130, 17-22. DOI: 10.1016/j.supflu.2017.07.018

Mira, I., Andersson, M., Boge, L., Blute, I., Carlsson, G., Salminen, K., Lappalainen, T., and Kinnunen, K. (2014). "Foam forming revisited. Part I. Foaming behaviour of fibre-surfactant systems," *Nordic Pulp & Paper Research Journal* 29, 679-688. DOI: 10.3183/NPPRJ-2014-29-04-p679-689

Nechita, P, and Năstac, S. (2022). "Overview on foam forming cellulose materials for cushioning packaging applications," *Polymers* 14(10), article 1963. DOI: 10.3390/polym14101963

Nechita, P., and Năstac, S. (2018). "Foam-formed cellulose composite materials with potential applications in sound insulation," *Journal of Composite Materials* 52(6), 747-754. DOI: 10.1177/0021998317714639

Nguyen, S., Feng, J., Ng, S., Wong, J., Tan, V., and Duong, H. (2014). "Advanced thermal insulation and absorption properties of recycled cellulose aerogels," *Colloids and Surfaces A: Physicochemical Engineering Aspects* 445, 128-134. DOI: 10.1016/j.colsurfa.2014.01.015

Notario, B., Pinto, J., Solorzano, E., de Saja, J., Dumon, M., and Rodríguez-Pérez, M. (2015). "Experimental validation of the Knudsen effect in nanocellular polymeric foams," *Polymer* 56, 57-67. DOI: 10.1016/j.polymer.2014.10.006

Ottenhall, A., Seppanen, T., and Ek, M. (2018). "Water-stable cellulose fiber foam with antimicrobial properties for bio based low-density materials," *Cellulose* 25(4), 2599-2613. DOI: 10.1007/s10570-018-1738-y

Pääkkönen, E., Ketoja, J, and Paltakari, J. (2024). "Energy absorption and resilience in quasi-static loading of foam-formed cellulose fibre materials," *Cellulose* 31(11), 7137-7152. DOI: 10.1007/s10570-024-06030-4

Pääkkönen, E., Prakash, B., Siilasto, R., and Kiiskinen, H. (2023). "High consistency foam in pilot scale," in: *TAPPICon 2023*, Atlanta, GA, USA.

Paunonen, S., Keränen, J., and Kamppuri, T. (2024). "Air-laid and foam-laid nonwoven composites: The effect of carrier medium on mechanical properties," *Journal of Applied Polymer Science* 141, article ID 202141. DOI: 10.1002/app.55986

Pöhler, T., Jetsu, P., and Isomoisio, H. (2016). "Benchmarking new wood fibre-based sound absorbing material made with a foam-forming technique," *Building Acoustics* 23(3-4), 131-143. DOI: 10.1177/1351010X16661564

Pöhler, T., Jetsu, P., Fougerón, A., and Barraud, V. (2017). "Use of papermaking pulps in foam-formed thermal insulation materials," *Nordic Pulp & Paper Research Journal* 32(3), 367-374. DOI: 10.3183/NPPRJ-2017-32-03-p367-374

Pöhler, T., Ketoja, J. A., Lappalainen, T., Luukkainen, V.-M., Nurminen, I., Lahtinen, P., and Torvinen, K. (2020). "On the strength improvement of lightweight fibre networks by polymers, fibrils and fines," *Cellulose* 27(12), 6961-6976. DOI: 10.1007/s10570-020-03263-x

Russel, S. (2006). *Handbook of Nonwovens, The Textile Institute Series*, Elsevier, Amsterdam, Netherlands.

Scheiding, W. (2000). "Thermal conductivity of wood fibers for insulation panels," *Holz als Rohund Werkstoff* 58(3), 0177-0181.

Seantier, B., Bendahou, D., Bendahou, A., Grohens, Y., and Kaddami, H. (2016). "Multi-scale cellulose based new bio-aerogel composites with thermal super-insulating and tunable mechanical properties," *Carbohydrate Polymers* 138, 335-348. DOI: 10.1016/j.carbpol.2015.11.032

Seciureanu, M., Năstac, S.-M., Guiman, M.-V., and Nechita, P. (2023). "Cellulose fibres-based porous lightweight foams for noise insulation," *Polymers* 15(18), article 3796. DOI: 10.3390/polym15183796

Siljander, S., Keinänen, P., Ivanova, A., Lehmonen, J., Tuukkanen, S., Kanerva, M., and Björkqvist, T. (2019). "Conductive cellulose based foam formed 3D shapes – From innovation to designed prototype," *Materials* 12(3), article 430. DOI: 10.3390/ma12030430

Uetani, K., and Hatori, K. (2017). "Thermal conductivity analysis and applications of nanocellulose materials," *Science and Technology of Advanced Materials* 18(1), 877-892. DOI: 10.1080/14686996.2017.1390692

Viitala, J., Lappalainen, T., and Jarvinen, M. (2020). "The use of co-surfactant to prevent the precipitation of an anionic surfactant in foam forming," in: *Progress in Paper Physics Seminar: PPPS2020*, Jyväskylä, Finland, pp. 293-295.

Wagner, M., Biegler, V., Wurm, S., Baumann, G., Nypelö, T., Bismarck, A., and Feist, F. (2025). "Pulp fibre foams: Morphology and mechanical performance," *Composites Part A: Applied Science and Manufacturing* 188, article ID 108515. DOI: 10.1016/j.compositesa.2024.108515

Walle, W., and Janssen, H. (2019). "Impact of pore scale parameters on the thermal conductivity of porous building blocks," *MATEC Web of Conferences* 282, article 02012 CESBP 2019.

Zhu, Y., Zhu, J., Yu, Z., Ye, Y., Sun, X., Zhang, Y., Zhu, P., and Jiang, F. (2022). "Air drying scalable production of hydrophobic, mechanically stable, and thermally insulating lignocellulosic foam," *Chemical Engineering Journal* 450(3), article 138300. DOI: 10.1016/j.cej.2022.138300

Article submitted: May 15, 2025; Peer review completed: September 16, 2025; Revised version received and accepted: October 11, 2025; Published: October 30, 2025.
DOI: 10.15376/biores.20.4.10922-10958

SUPPLEMENTARY INFORMATION

APPENDIX 1
A-type and B-type Fines

The fibre length, fibre width, gravimetric coarseness, and the percentages of the A-type and B-type fines (flakes and fibrils type elements, see Fig. 1) were measured with the FS5 Fibre Image Analyzer (Valmet Automation, Kajaani, Finland). Note that the FS5 measures the fractions optically so that fines A is calculated as a percentage of the projection area of particles, and fines B is calculated as a percentage of particle length.

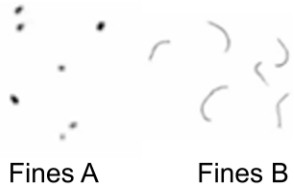

Fig. A1. Images of flakes-like A-type fines and fibrils-like B-type fines (Cecchini *et al.* 2024)

Cecchini, J., Koponen, A., Laukkanen, O.-V. and Jäsberg, A. (2024). "Alternative methods to evaluate flocculation of particles in papermaking suspensions," *TAPPI Press, Proceedings of TAPPICon 2024*, April 28-May 1, 2024, Cleveland OH, USA, https://imisrise.tappi.org/TAPPI/Products/24/TAP/24TAP168.aspx

APPENDIX 2
Calculating the Fibre Properties of the 50% - 50% Acacia-BSKP Mixture

For the acacia-BSKP mixture, the average coarseness was estimated from the formula

$$\omega = \frac{2\omega_1\omega_2}{\omega_1 + \omega_2},$$

the average fibre length was estimated from the formula

$$L = \frac{\omega_2 L_1 + \omega_1 L_2}{\omega_1 + \omega_2},$$

and the average fibre width was estimated from the formula

$$w = \frac{\omega_2 w_1 + \omega_1 w_2}{\omega_1 + \omega_2}.$$

The above indexes 1 and 2 refer to the acacia and BSKP furnish, respectively. The Fines A and Fines B content of the acacia-BSKP mixture were calculated with the arithmetic mean of the Fines A and Fines B contents.

APPENDIX 3
Measurement Methods

X-ray tomography

X-ray microtomography produces a three-dimensional (3D) volume image of the fine-scale structure of the studied object. The output of the imaging process is a volume

image, where contrast originates from differences in local X-ray attenuation in the sample, which correlates with the local material density. The obtained 3D X-ray attenuation maps can be binarised into the void (air) and fibre phases by choosing a suitable threshold value. In this work, tomographic images were obtained using a Rx Solutions Desktom 130 tomography scanner (Chavanod, France). Samples were imaged using 40 kV X-ray tube voltage and 8 W electron beam power. The voxel size was 11.8 µm and 1440 projection images were collected from each sample over 360°. The exposure time was 2 s, and two projection images were averaged per angular step. The sample was imaged in three parts with stacked projections. This resulted in a total imaging time of approximately 75 min for one sample. The projections were reconstructed into volume images using the filtered back projection algorithm and visualised using Voreen software (Drees D., & Leistikow S., version 5.0, Universität Münster, Münster, Germany). Fibre orientation profiles, porosity profiles, pore size distributions, and geometric tortuosities were calculated for the materials from the binarized volume images. The images had to be scaled down to the voxel size of approximately 24 µm for the calculations due to the large file size of the volume images.

The pore size distribution of binarised X-ray images of the samples was estimated by fitting maximum-sized spheres into the void space that did not include the fibre phase. As an outcome, each voxel in the 3D space of the image was labelled with the diameter of the maximal sphere to which it belonged. To measure the mean pore diameter, the fitted sphere diameter values were integrated over the void space and divided with the total void volume. Similarly, the mean pore size at each z-position could be determined. The fibre orientation was calculated using the structure tensor method, utilising convolution with Gaussian kernel (sigma = 1) for derivatives and the weight in the structure tensor. Geometric tortuosity in the void and solid phases was calculated as the ratio of effective path length to sample thickness, where paths were traced as the shortest connections from one side of the sample to the opposite side. Note that the porosity values calculated from the binarised images are more sensitive to the X-ray image resolution and image thresholding than the pore sizes (Keränen *et al.* 2023). Typically, unless the image resolution is high enough, the sample porosities obtained from the tomographic images are lower than the real sample porosities.

Thermal conductivity measurements

The problem of comparing the thermal conductivities presented in different papers is that the obtained results may depend on the measurement method and the sample size. Most methods have been developed for continuum materials, whereas the natural fibre-based materials are homogeneous only in large enough scale and with thick enough samples. Thus, one is advised to adopt standard methods specifically designed for studying traditional insulation materials. A well-established device here is the heat flow meter (HFM), which can be used to measure thermal conductivities of building materials with the EN 12667 (2001) standard.

The accuracy of the measured thermal conductivity was tested with several commercial insulation material measurements for 30 cm × 30 cm samples (See Table A1). For an XPS sample, *e.g.*, the manufacturer-stated thermal conductivity was 34 mW/m·K, which was in excellent agreement with the measured value of λ = 34.3 mW/m·K.

The thermal conductivity of insulation materials was measured with the heat flow meter HFM Fox314. The chamber size of the HFM Fox314 device is 30 cm × 30 cm, but the actual measurement area is 10 cm × 10 cm, and one can measure thermal conductivity for rather small samples. In such measurements, the rest of the chamber is filled with

insulation material. We used foam rubber for this purpose, the thermal conductivity of which was measured to be 38.6 mW/m·K. This approach was tested with a 15 cm × 15 cm XPS sample. The measured thermal conductivity was 35.9 mW/m·K, which was 5% higher than the correct value. When a 15 cm × 15 cm rubber foam sample was surrounded with a 30 cm × 30 cm XPS sample, the measured thermal conductivity for the rubber foam was 2% higher, namely 39.3 mW /m·K. The reason may have been the rubber foam being slightly thinner than XPS. Thus, there were thin air layers on the rubber foam surfaces through which the transport of thermal energy by thermal radiation was efficient (air pockets were found to generally increase the measured thermal conductivity). Another possibility is that there may have been some air conduction through voids in the contact area of the rubber foam and XPS. Thus, it is likely that the measured thermal conductivities of the 15 cm × 15 cm samples, used in this study, are usually slightly higher than the real values.

Table A1. Measured Thermal Conductivities of Various Commercial Insulation Materials*

Material	Thickness	Density	Thermal conductivity	Manufacturer-stated
	(mm)	(kg/m^3)	(mW/mK)	(mW/mK)
XPS	31	34.4	34.3	34
rock wool	50	34.3	35.4	36
glass wool	48	16.5	35.3	36
glass wool	50	22.5	34.3	33
recycled wood fibres	45	45.8	38.8	39

*Note: Measurements were performed for 30 cm × 30 cm samples. The thickness of the samples varied between 30 mm and 50 mm.

To demonstrate the potential problems of using a non-standard method, the authors tested the applicability of the hot disk method (HDM) for these materials. HDM is quite popular in the field of materials science and engineering. The measurement is based on the Transient Plane Source (TPS) method (Log and Gustafsson 1995), where a heat pulse is used for measuring the thermal conductivity. According to the Hot Disk® manual this method "is the most precise and convenient technique for studying thermal transport properties in accordance with ISO 22007-2". Figure A1 shows the measuring setup of the Hot Disk (HD) device for measuring the thermal conductivity. In the present measurements the Hot Disk TPS 2500 was used, and the diameter of the disc was 9.9 mm.

There is a fundamental difference between the heat flow meter (HFM) and hot disk methods. In the HFM method, the heat flow is one-dimensional and the method measures the (average) thermal conductivity of the whole insulation panel. In the HD method, the heat flow is three-dimensional, and the measurement is local (only the parts of the material that are rather close to the sensor affect the measured thermal conductivity). For insulation in buildings, heat flow takes place mainly in one direction – perpendicularly to the panel surfaces. The HFM method is thus more relevant for most practical insulation purposes. The problem with HDM is that the obtained thermal conductivities do not necessarily reflect the performance of the insulation material for real-life purposes. For instance, the fibres in the foam-formed natural fibre-based materials are strongly aligned and thermal conductivities are different in the planar and cross-plane directions (see Fig. A2). Moreover, foam-formed materials are not necessarily homogeneous – there may be

differences *e.g.* in the local fibre density. The 3D effect is likely to decrease with increasing sensor size. Figure A3 compares the thermal conductivities of cellulosic fibrous materials with variable density measured with the HD and HFM methods. It is apparent that there was a big discrepancy between the measured thermal conductivities and the difference increases with increasing sample density. HD method is thus unsuitable for measuring the thermal conductivity of cellulosic lightweight fibrous materials. This might be the case also for some other methods used for thermal insulation measurements (Log and Gustafsson 1995).

Log, T. and Gustafsson, S. (1995). "Transient plane source (TPS) technique for measuring thermal transport properties of building materials," *Fire and Materials* 19(1), 43–49.

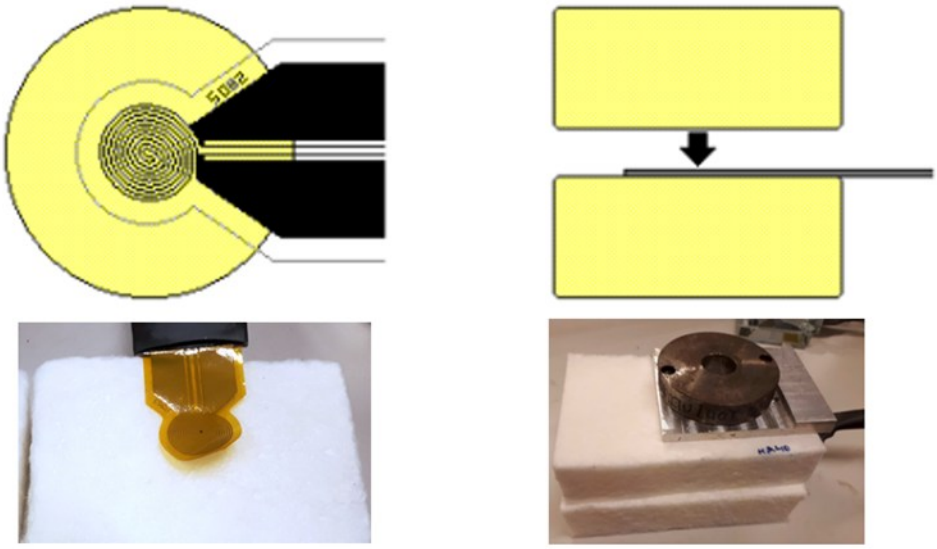

Fig. A1. The hot disk method for measuring thermal conductivity. The disk is placed between two samples of the studied material.

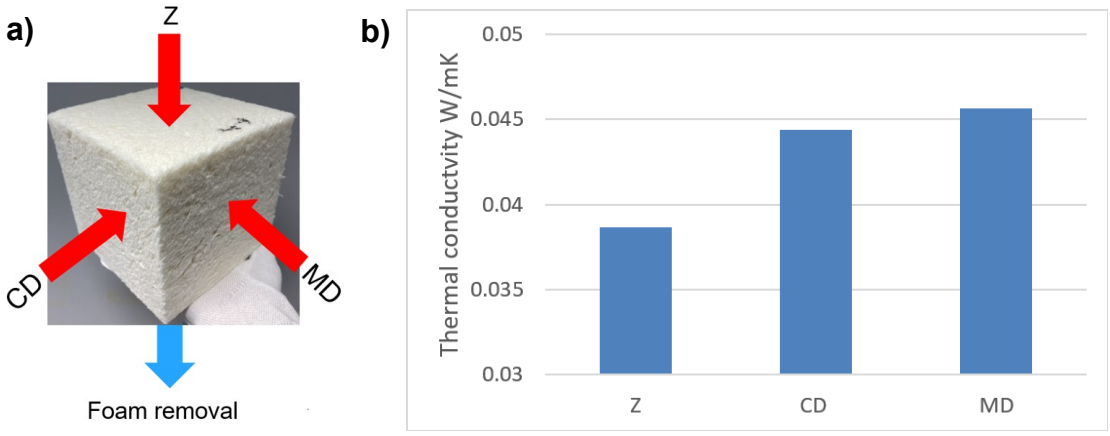

Fig. A2. Thermal conductivity of a foam-formed cellulosic fibre sample measured in different directions. Thermal conductivity was 15 to 20% smaller in the z-direction (foam removal direction). Thermal conductivity was highest in the MD direction, *i.e.*, in the direction of the flow of foam in the mould. The side length of the cube is 15 cm and density is 40 kg/m^3. The measurements were performed for 5 × 15 × 15 cm^3 samples cut from three identical cubes.

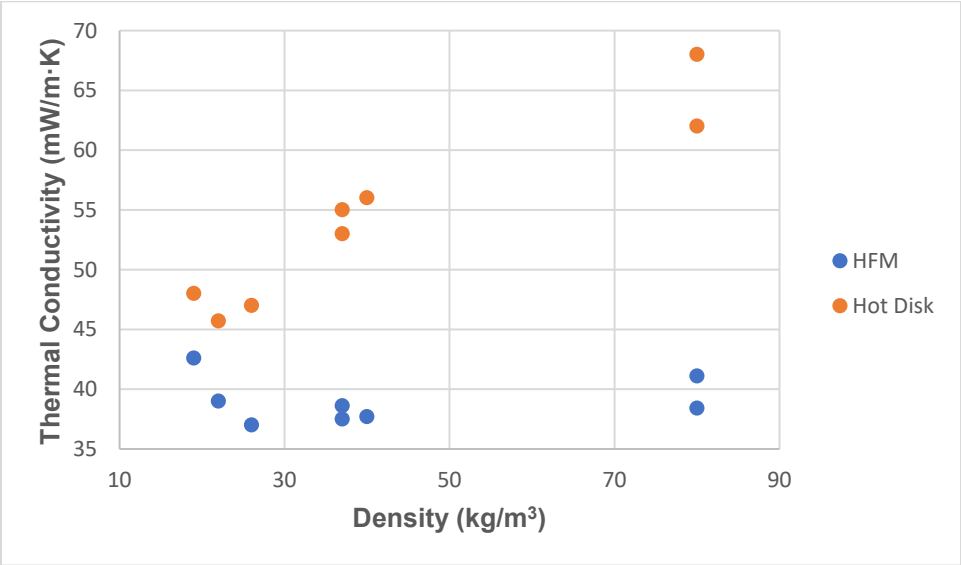

Fig. A3. Comparison of thermal conductivity measured with HD and HFM methods for different cellulose-based insulation materials

APPENDIX 4
X-ray Tomographic Images

The xz, yz, and xy-planes were taken from the sample middle. The sizes for the xz, yz- and xy-planes were *ca.* 2 cm × 3 cm, 2 cm × 3 cm and 2 cm × 2 cm, respectively.

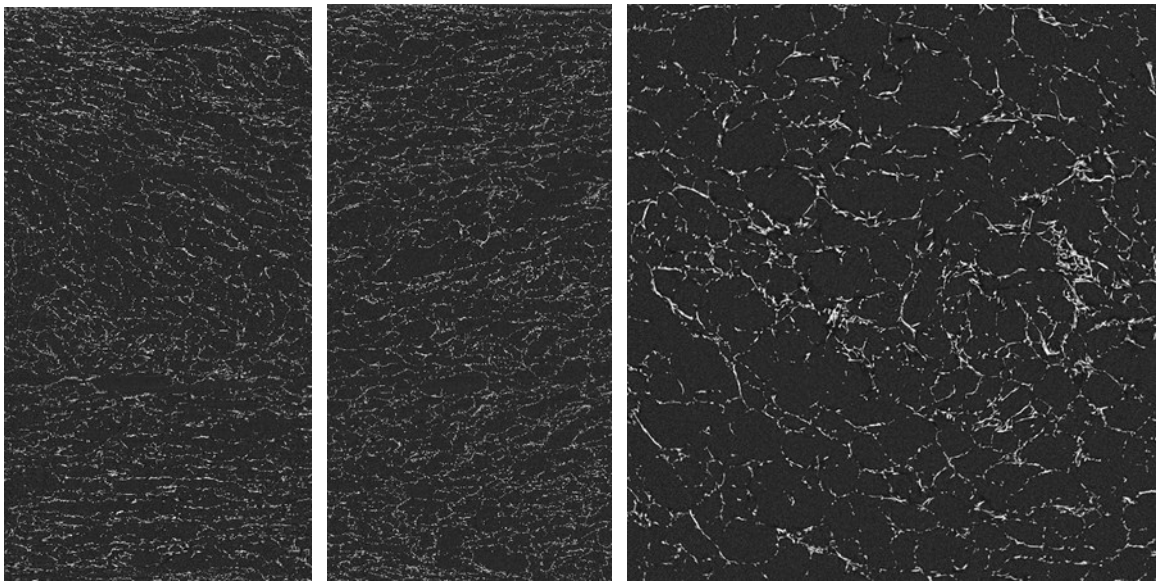

Fig. A1. BSKP, xz-plane, yz-plane, and xy-plane

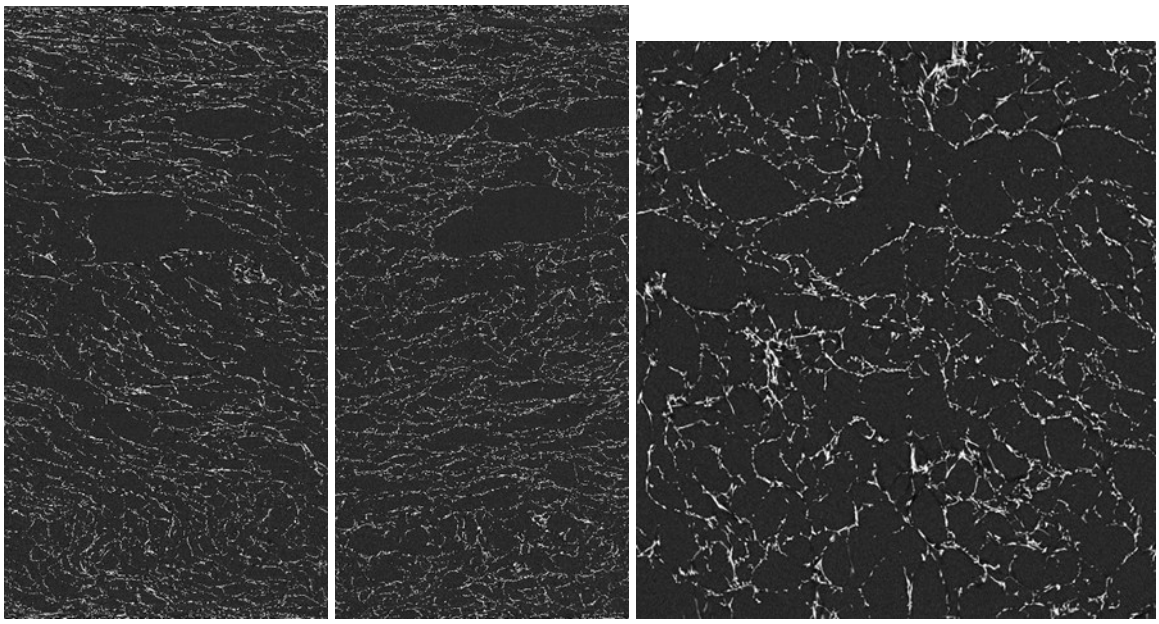

Fig. A2. BSKP SR23, xz-plane, yz-plane, and xy-plane

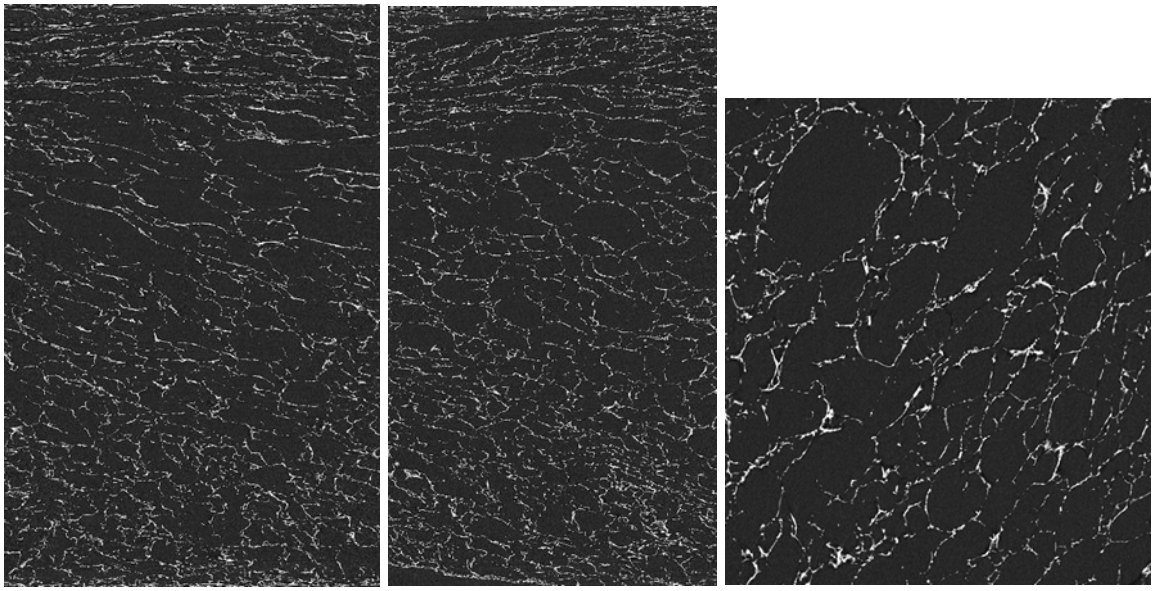

Fig. A3. BSKP SR89, xz-plane, yz-plane, and xy-plane

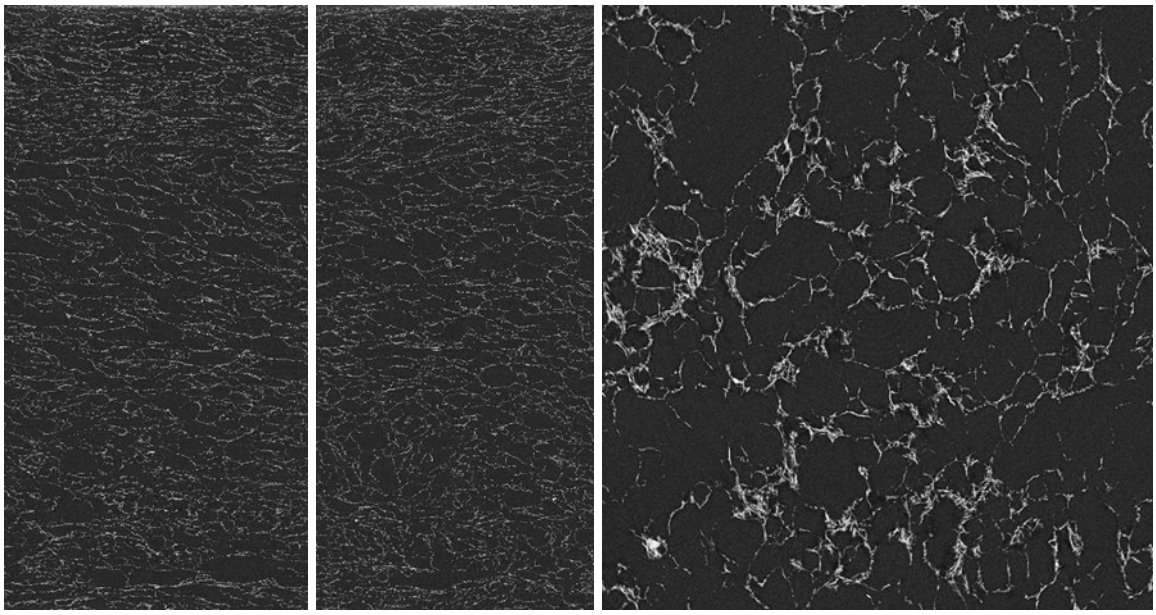

Fig. A4. Acacia, xz-plane, yz-plane, and xy-plane

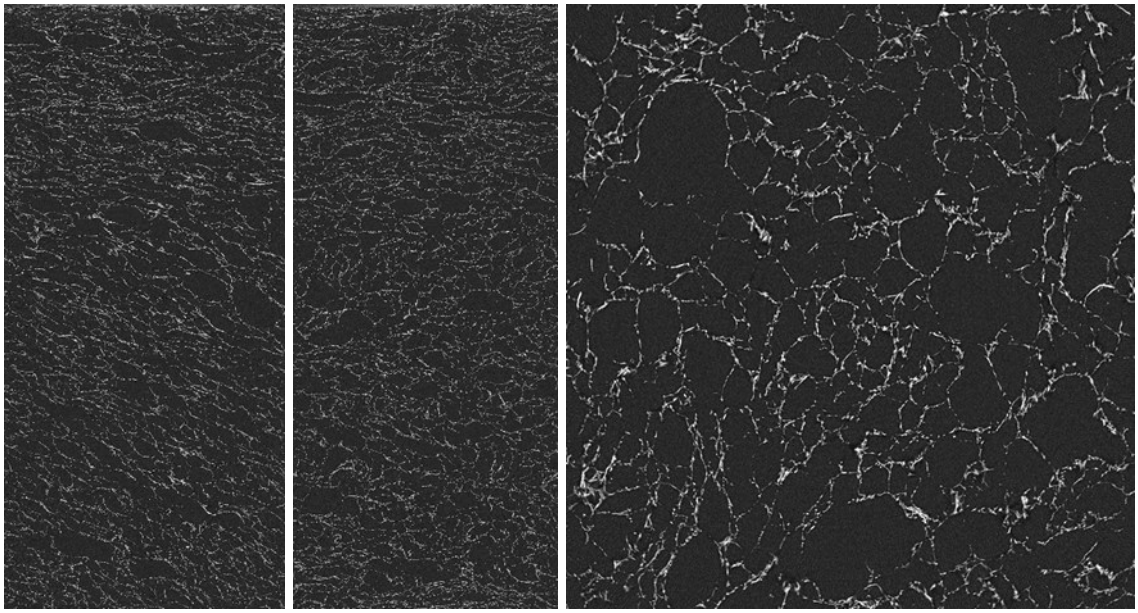

Fig. A5. Acacia 50% + BSKP 50%, xz-plane, yz-plane, and xy-plane

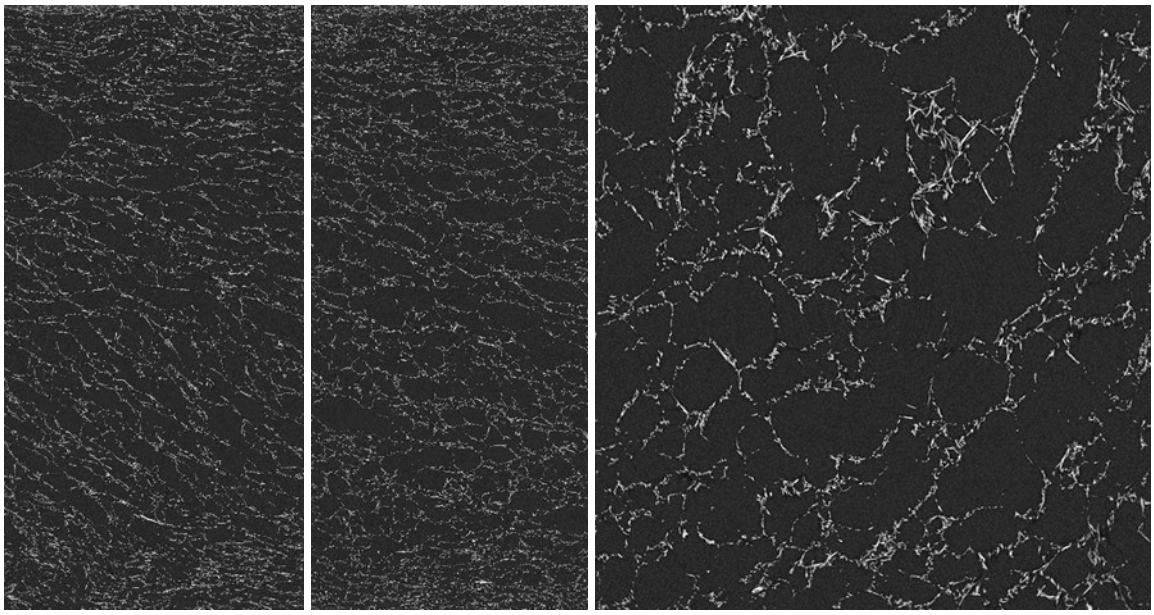

Fig. A6. CTMP, xz-plane, yz-plane, and xy-plane

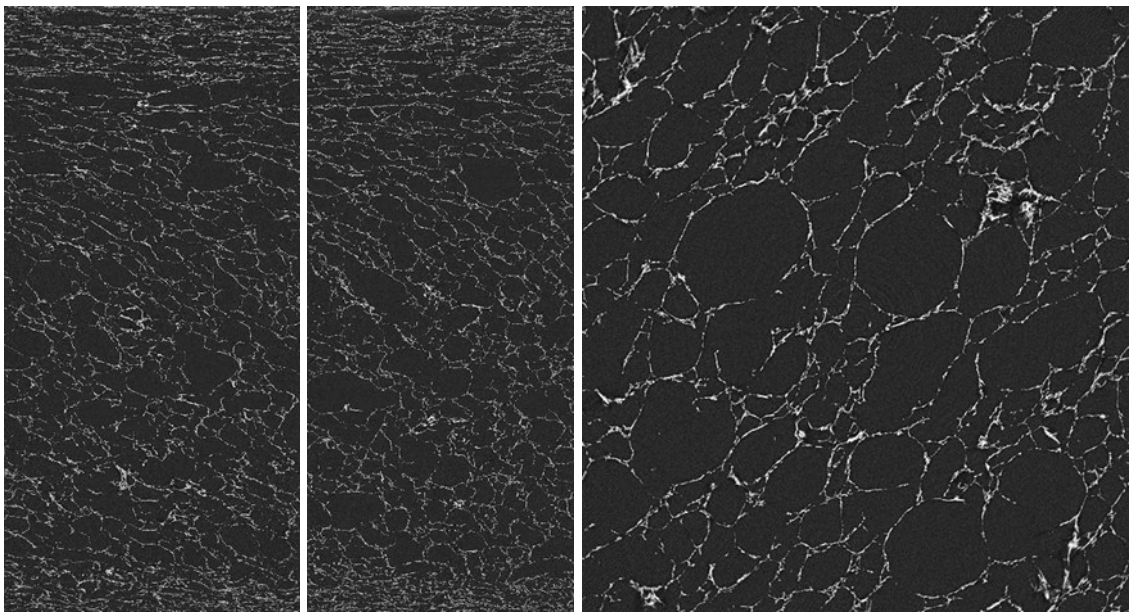

Fig. A7. Highly refined CTMP, xz-plane, yz-plane, and xy-plane

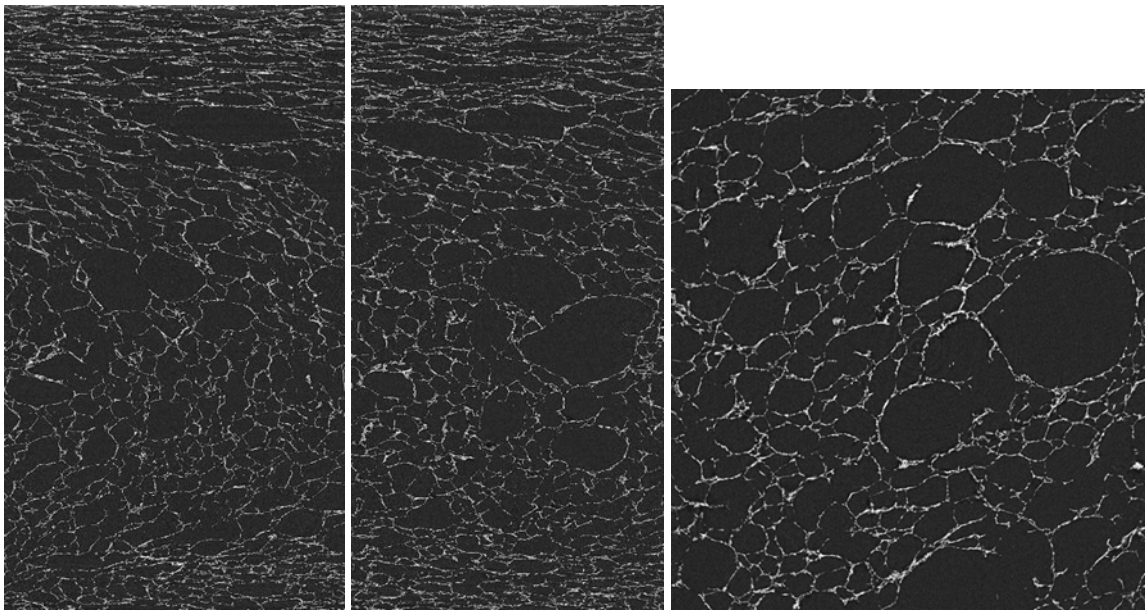

Fig. A8. Highly refined CTMP + TEMPO 4%, xz-plane, yz-plane, and xy-plane

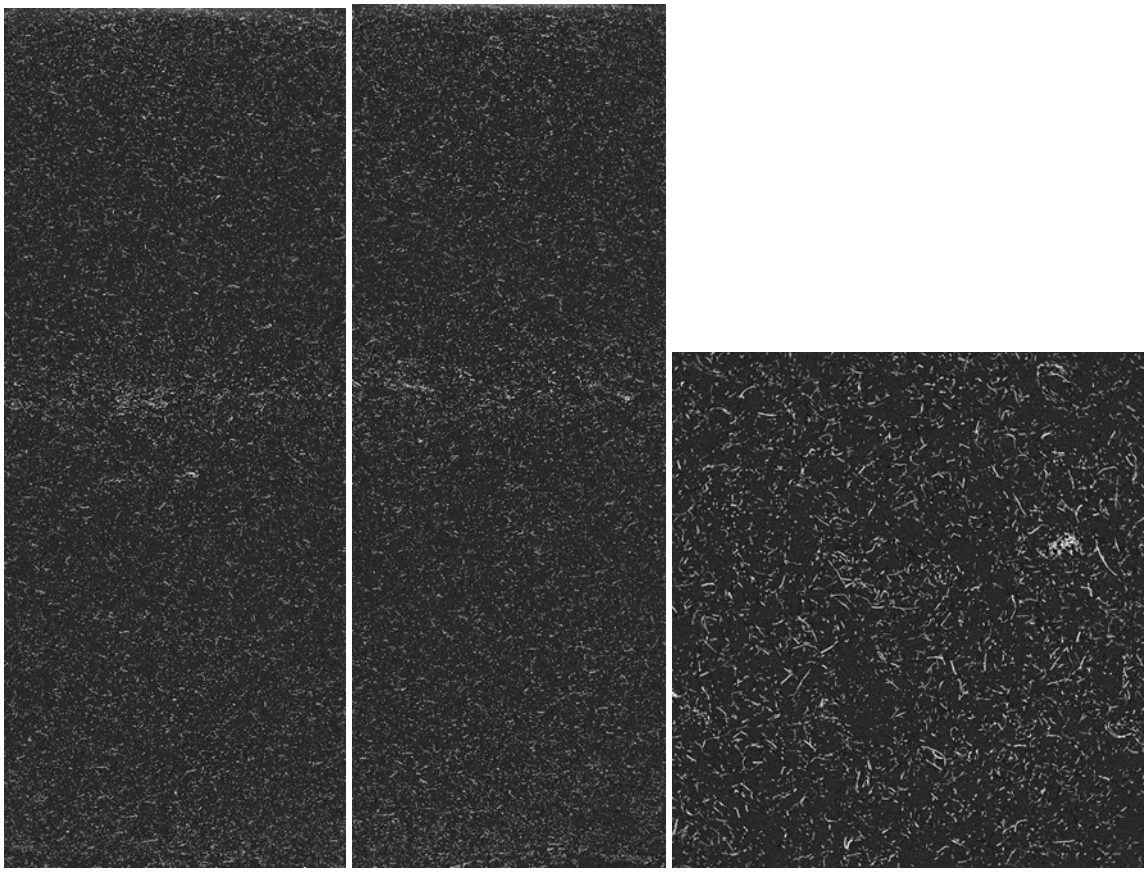

Fig. A9. BSKP fluff-30, xz-plane, yz-plane, and xy-plane

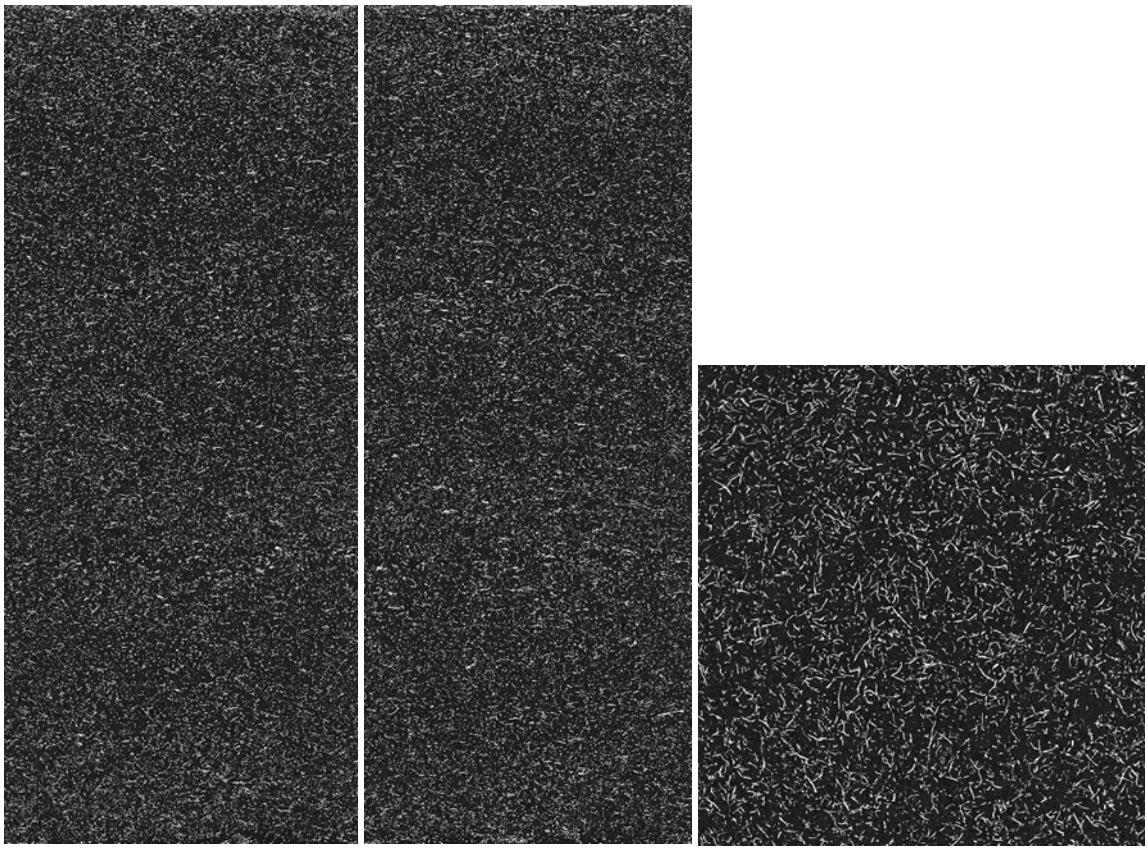

Fig. A10. BSKP fluff-40, xz-plane, yz-plane, and xy-plane.

APPENDIX 5
Pore Size Distributions of Foam-formed Samples

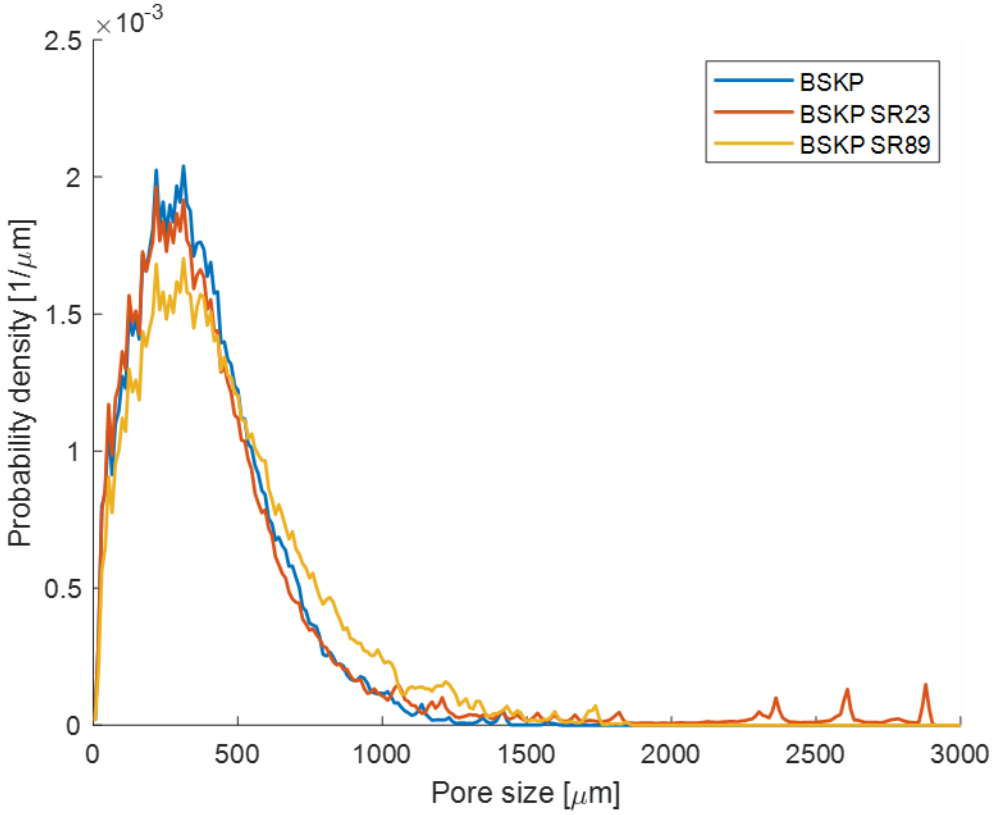

Fig. A1. Pore size distributions of BSKP, BSKP SR23, and BSKP SR89

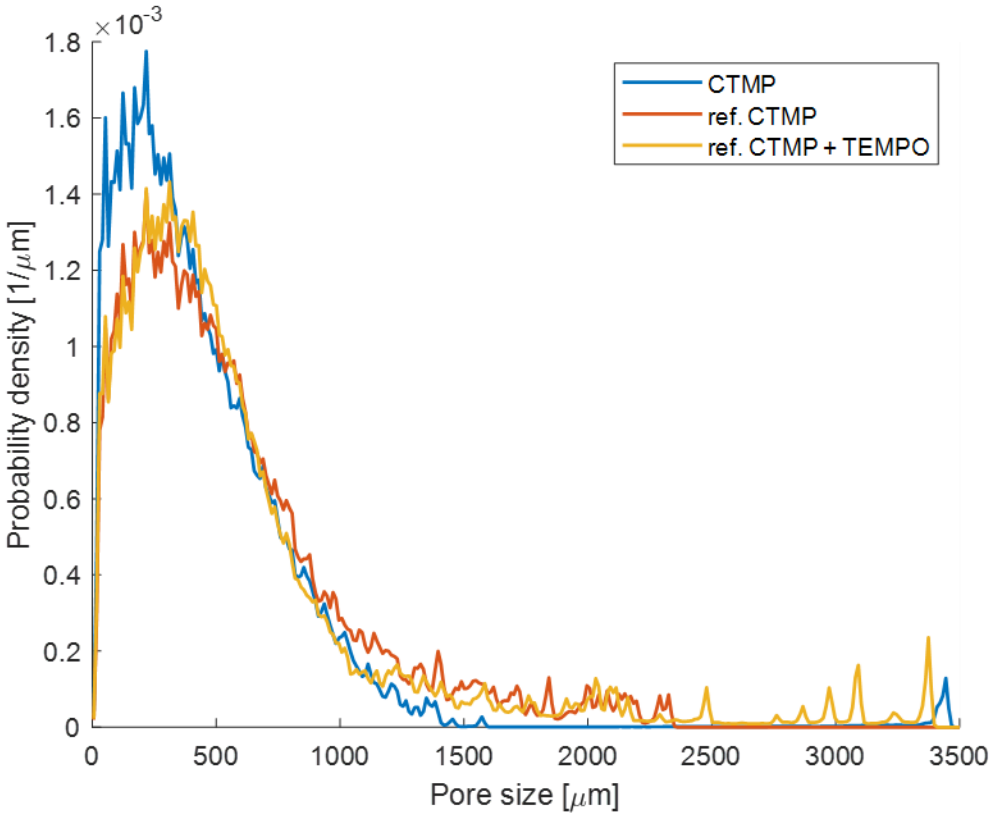

Fig. A2. Pore size distributions of CTMP, refined CTMP, and refined CTMP + TEMPO

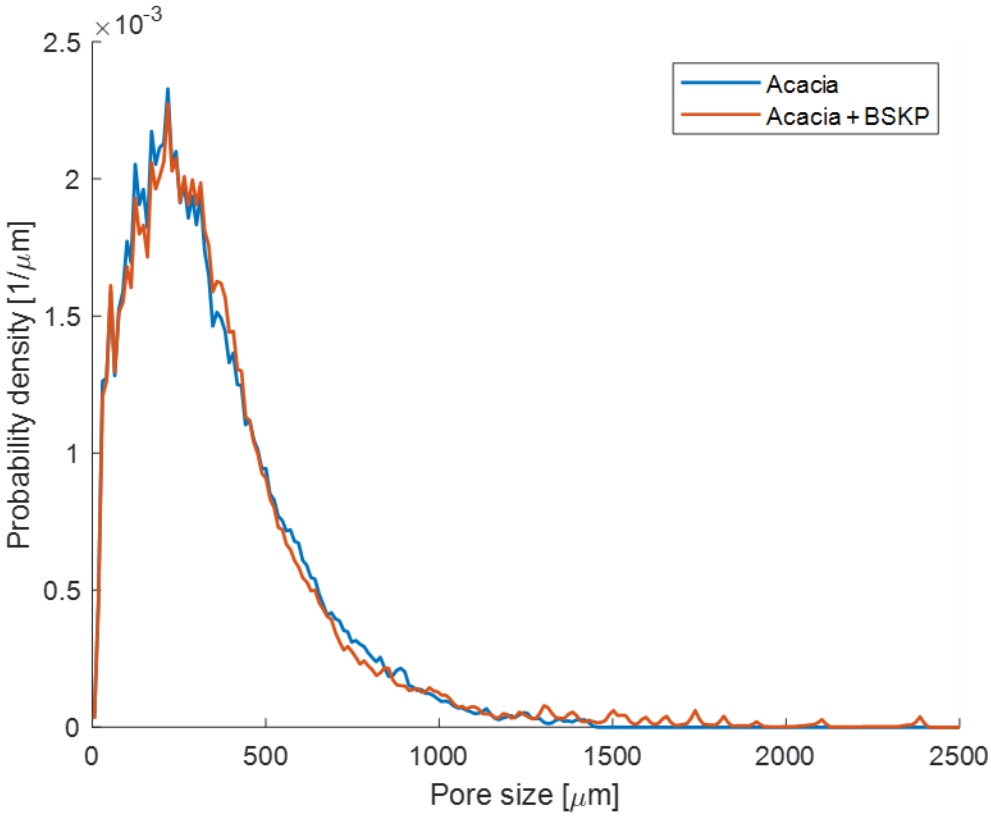

Fig. A3. Pore size distributions of acacia, and acacia + BSKP